Chemical Science

Accepted Manuscript

This article can be cited before page numbers have been issued, to do this please use: H. Yu, Z. Wang, M. Li, M. Hu, J. Yang, R. Li, B. Wang, G. Zhao, X. Wang, X. Yan, Y. Hao, H. Ma and J. Liu, *Chem. Sci.*, 2025, DOI: 10.1039/D5SC02677F.

ROYAL SOCIETY OF CHEMISTRY

rsc.li/chemical-science

View Article Online
DOI: 10.1039/D5SC02677F

High-capacity aqueous imidazolium-ion battery enabled by MMZ-H^+/H^+ co-intercalation in a near neutral electrolyte

Haiping Yu,[a,b] Rui Li,[a,b] Zhihui Wang,[c] Bei Wang,[a,b] Mengxiao Li,[c] Guoqing Zhao,[c] Xinyu Wang,[a,b] Xiaorong Yan,[c] Yuxin Hao,[a,b] Huige Ma,[a,b] Jingru Liu,[a,b] Mingjun Hu,[,c] Jun Yang[*,a,d]*

a Beijing Institute of Nanoenergy & Nanosystems, Chinese Academy of Sciences, Beijing, 101400, China.

b School of Nanoscience and Engineering, University of Chinese Academy of Sciences, Beijing,101408, China.

c School of Materials Science and Engineering, Beihang University, Beijing 100191, China.

d Shenzhen Institute for Advanced Study, University of Electronic Science and Technology of China, Shenzhen, 518000, China.

[*]Corresponding author, E-mail: mingjunhu@buaa.edu.cn, yangjun@binn.cas.cn.

Abstract:

Rechargeable aqueous batteries are regarded as promising candidates for large-scale energy storage with the advantages of cost-effectiveness, environmentally friendliness, and innate safety. However, to date, most of the aqueous ion batteries that have been reported are equipped with metal cation charge carriers and encounter either poor sustainability or low reaction activity. Here, we first reported an aqueous imidazolium-ion battery with MMZ-H^+/H^+ as co-intercalated ions. In detail, we configured an almost neutral electrolyte with a wide electrochemical window of 2.66 V by adding an appropriate amount of alkaline 1-methylimidazole (MMZ) to 0.5 M H_2SO_4, named as 50M-10S electrolyte. Due to the strong binding energy between MMZ and H^+, the

MMZ-H^+ as an entire unit can insert into or extract from HATN-3CN (hexaazatrinaphthalene-2,8,14-tricarbonitrile) electrode. The MMZ-H^+ and H^+ co-insertion increases the capacity by 40% compared to pure H^+ insertion in this proton battery (287.6 mAh g^{-1} in 50M-10S electrolyte vs. 206.8 mAh g^{-1} in 0.5 M H_2SO_4 electrolyte, 0.1 A g^{-1}). Theoretical calculations illustrated that the insertion of MMZ-H^+ can further activate the unreacted N active sites due to their enhanced nucleophilicity derived from stronger electron-donating ability of ionized nitrogen sites than the protonated one. Moreover, the assembled full batteries also exhibit ultra-high specific capacity (266.6 mAh g^{-1}, 1 A g^{-1}) and ultra-slow degradation (capacity retention of 97 %, 1 A g^{-1}, 1000 cycles). This research further enriches the library of inserted ions and will help to understand and enhance proton storage in near-neutral electrolytes and build new battery model.

Keywords: near-neutral electrolyte, high capacity, organic electrode, aqueous imidazolium-ion battery, MMZ-H^+ (de)insertion.

Introduction

Rechargeable batteries are attracting widespread attention due to the increasing depletion of fossil fuels.[1, 2] Up to now, metal ion batteries, especially Li-ion batteries (LIBs) with non-aqueous electrolytes, have been applied in portable electronics and electric vehicles, for their high energy density and satisfactory cycle life.[3-5] However, lithium as a scarce resource in nature limits the further development of LIBs.[6] Although sodium-ion batteries (SIBs) and potassium-ion batteries (KIBs) with earth-abundant elements as charge carriers are promising candidates,[7, 8] the use of flammable electrolytes in these batteries may pose safety risks especially in extreme environments such as crash and needle puncture.[9] Hence, it is necessary to explore aqueous energy storage devices with low cost and high security.

Various aqueous batteries have emerged as a reliable alternative with high-level safety, outstanding rate performance, and low cost.[10-15] Among them, non-metal ion,

View Article Online
DOI: 10.1039/D5SC02677F

proton (H^+) and ammonium (NH^{4+}) ions, are considered as promising energy storage systems due to their sustainability.[16] However, the electrochemical window of aqueous electrolytes is limited by water decomposition potentials (1.23 V).[17] Although ammonium salt electrolytes are less prone to the hydrogen evolution reaction (HER) compared with strong acid electrolytes,[15] they are commonly afflicted with low electrochemical reaction activity, which gives rise to non-ideal electrode capacity. For protonic electrolytes, other problems that are often mentioned are the dissolution of electrode materials and corrosion of battery packaging materials.[18, 19] Recently, water-in-salt (WIS) electrolytes were also developed to widen the electrochemical window by restraining the content of free water, but high viscosity and cost stifled their development potential.[20, 21] Similar to the WIS strategy, water-in-acid (WIA) electrolytes with high ionic conductivity have recently been reported. The MoO_3 electrode exhibited a high reversible capacity and excellent cycling stability in a 9.5 M H_3PO_4 electrolyte, fully demonstrating the promising potential of the WIA electrolyte for proton energy storage. However, the corrosiveness of high-concentration H_3PO_4 to metal components and the human body should still not be ignored.[22] Besides, a water-free electrolyte of H_3PO_4/MeCN was proposed to inhibit hydrogen evolution reaction, but poor compatibility between H_3PO_4 and MeCN results in unstable electrochemical properties of proton battery.[23] The ionic liquids electrolytes had also been widely researched because of their chemical stability and easy synthesis.[24, 25] Nevertheless, the low ion transport rate and high cost limit their popularization.[26] Solid electrolytes have the prospect of commercialization, but the ion transfer efficiency needs to be improved because of the poor interfacial wettability between the electrolyte and the electrode.[27] The addition of organic solvents to aqueous electrolytes is regarded as a useful strategy to broaden electrochemical stability window while maintaining their non-flammability.[28] However, due to relatively weak electron-donating ability, most organic solvents showed a very limited influence on proton activity and hydrogen evolution side reaction of aqueous-organic hybrid electrolyte. Unlike previously reported organic additives, 1-methylimidazole (MMZ) is a potent organic alkali (pKa=6.95), which can show a strong interaction with proton and thus well regulate proton activity of hybrid

View Article Online
DOI: 10.1039/D5SC02677F

electrolytes to inhibit hydrogen evolution and electrode corrosion. However, the intense interaction between MMZ and H^+ ions also suppresses their dissociation and produces a large amount of MMZ-H^+ cations in aqueous electrolytes. Compared to NH_4^+, MMZ-H^+ has a larger size but higher electrode wettability due to the fact that MMZ reduces the interfacial energy between the electrode material and the liquid electrolyte, may better arousing the capacity of the electrode.[29] Therefore, it is important to investigate such an aqueous imidazolium-ion battery, not only helping to understand the unique charge storage mechanism in such a proton-pump-like electrolyte, but also promoting the battery performance.

Herein, we configured an electrolyte by an acid-alkali coordinated regulation strategy. The almost neutral electrolyte was prepared by adding a small amount of alkaline MMZ to 0.5 M H_2SO_4, named as M-S electrolytes. Compared to 0.5 M H_2SO_4, the optimized M-S electrolyte, 50M-10S with the molar ratio of MMZ to H_2SO_4 5:1, had an 0.71 V wider operating voltage window due to the entrance of MMZ into the solvation sheath of H^+. In addition, this electrolyte with near-neutral pH value provided a mildest chemical environment, and reduced the chemical dissolution of the electrode materials. More importantly, we found that MMZ could be inserted into the HATN-3CN electrode after protonation (MMZ-H^+), (Figure 1), which, to the best of our knowledge, is the largest inserted cations reported to date for energy storage (Figure S1 and Table S1). A series of characterizations had verified the co-insertion of MMZ-H^+ and H^+ during electrochemical reactions. The capacity of HATN-3CN electrode has been increased by 40% compared to pure H^+ insertion (287.6 mAh g^{-1} in 50M-10S electrolyte vs. 206.8 mAh g^{-1} in 0.5 M H_2SO_4 electrolyte, 0.1 A g^{-1}), and also far exceeded the capacity in 1 M $(NH)_2SO_4$, another near-neutral electrolyte (Figure S2). The full batteries were assembled by using the MnO_2 as the cathode, the HATN-3CN as the anode and 0.5 M $MnSO_4$+50M-10S as the electrolyte. The high capacity (266.6 mA h g^{-1}, 1 A g^{-1}) and excellent capacity retention (97 % capacity retention, 1 A g^{-1}, 1000 cycles) were achieved. This work is expected to provide valuable insights and impetus for the development of mild and effective aqueous battery electrolytes.

View Article Online
DOI: 10.1039/D5SC02677F

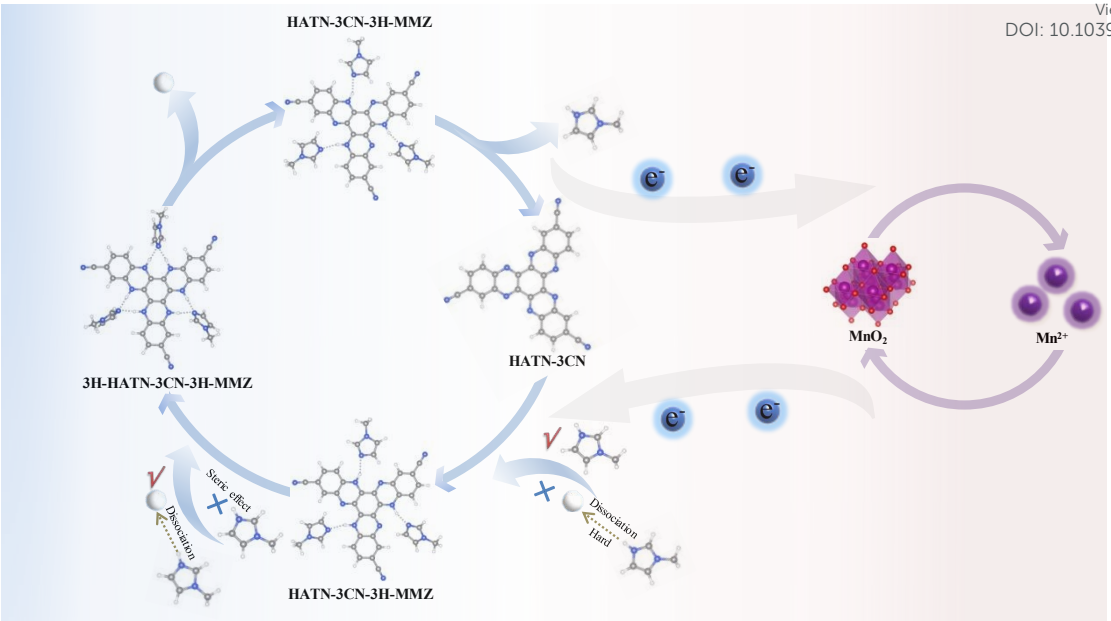

Figure 1. Scheme of simplified electrochemical process.

Results and Discussion

Electrolyte design and discussion

Different ratio of MMZ was added to 0.5 M H_2SO_4 and fully stirred to formulate the stable electrolytes. The detailed molar ratios of each component and pH values of the electrolytes are displayed in Table S2. The electrochemical impedance spectroscopy (EIS) was used to investigate the ionic conductivity of the electrolytes (Figure S3).[30, 31] Observably, the ionic conductivity of the 50M-10S electrolyte (254.4 mS cm^{-1}) was the highest among all the electrolytes, even better than that of the 0.5 M H_2SO_4 (219.6 mS cm^{-1}), maybe attributed to the increased types and quantities of cations as well as rich N sites on the MMZ for proton hopping.[32] Specifically, the introduction of methylimidazolium, as a weak base, can promote the secondary ionization of HSO_4^- and increase the ion number, further enhancing the ionic conductivity. Meanwhile, the conjugated imidazolium ring structure of methylimidazolium ions enables the delocalization of the positive charge, which effectively reduces the effective charge density of the cations, weakens the electrostatic attraction between cations and anions (e.g., HSO_4^-, SO_4^{2-}), and improves the ionic migration rate. However, excessive additions of MMZ would increase the resistance of ionic transport due to the enlarged

View Article Online
DOI: 10.1039/D5SC02677F

solvation structure and the increased solution viscosity, resulting in a decrease in ionic conductivity (Table S3 and S4).[33, 34] A series of the linear sweep voltammetry (LSV) curves of the electrolytes with different MMZ contents were measured and suggested that the electrochemical window of 0.5 M H_2SO_4 was significantly broadened after adding MMZ (Figure S4), but the extension rate gradually slowed down with increasing the MMZ content. Hence, taking both the ionic conductivity and electrochemical stability window into consideration, we selected this electrolyte with the molar ratio of MMZ to H_2SO_4 50:10 as the research focus in the following studies.

As shown in Figure 2a, the electrochemical stability window of 50M-10S electrolyte could attain to 2.66 V (from -1.07 V to 1.59 V vs. Ag/AgCl), with an extension of 0.71 V compared to 0.5 M H_2SO_4 (mainly in the anodic regions). To confirm the safety of aqueous-organic hybrid electrolyte, the combustion tests were carried out and indicated that the 50M-10S electrolyte was non-inflammable (Figure S5). Then the Fourier transform infrared (FTIR) spectra were performed to investigate the solution structure of the 50M-10S electrolyte (Figure 2b). Pure H_2O (gray line), H_2O spiked with MMZ (red line), and H_2O spiked with H_2SO_4 (blue line) served as controls for the 50M-10S electrolyte (green line). The peaks at 1522 cm^{-1} and 1108 cm^{-1} were attributed to imidazole ring skeleton vibration and stretching vibration.[35] Peaks at 1050 cm^{-1} and 1205 cm^{-1} correspond to the O=S=O stretching vibration of SO_4^{2-} [36]. The stretching and bending vibration of -CH_3 in MMZ could be observed in 2600~3100 cm^{-1} and 1300~1400 cm^{-1}.[35] The presence of these characteristic peaks indicated that each of raw materials was stabilized in the 50M-10S electrolyte. The Raman spectra similarly confirmed the presence of these characteristic peaks (Figure S6). The typical peaks at 3200~3700 cm^{-1} and 1550~1750 cm^{-1} represented the stretching vibration of HO-H and bending vibration of –OH.[36] The peak intensity of H_2O of 50M-10S electrolyte was the weakest, indicating that free water activity was limited by the interaction among components. The ^1H nuclear magnetic resonance (^1H-NMR) spectra of electrolytes also proved the same result (Figure 2c, d). The ^1H chemical shift in 7.52, 7.01 and 6.90 ppm represented the three C-H on the imidazole ring of MMZ. However, their respective movement to 7.94, 7.15 and 7.08 ppm in 50M-10S electrolyte

View Article Online
DOI: 10.1039/D5SC02677F

demonstrated that pyridinic N of MMZ captured H^+ from H_2SO_4. The electron-deficient characteristic of proton weakened the original electron cloud density of the imidazole ring in MMZ, which ensured an increase in the ^1H chemical shift of the MMZ in 50M-10S electrolyte.

Molecular dynamics (MD) simulations were performed to analyze the solvation structure of the 50M-10S electrolyte. As showed in Figure 2e, the snapshot of the 50M-10S electrolyte consisted of 40 H_2SO_4, 200 MMZ and 4320 H_2O molecules. To gain deeper insights into the solvation characteristics, the radial distribution functions (RDFs) were adopted, with the detailed results presented in Figure 2f. The H-N (MMZ), H-O (SO_4^{2-}) and H-O (H_2O) were well identified in the first solvation layer. Significantly, although only a small amount of MMZ was added into the 50M-10S electrolyte, the peak intensity of H-N (MMZ) was the highest, indicating organic alkali MMZ possessed powerful proton-binding capacity. By integrating the RDFs, the H^+ coordination numbers of the 50M-10S electrolyte were gained in Figure 2g. The average coordination number around a single H^+ was about 3.83 in 50M-10S electrolyte, with the contributions being 1.36 from MMZ, 2.11 from H_2O, and 0.36 from SO_4^{2-}, respectively. It indicated that even the modest addition of MMZ was sufficient to change the H^+ solvation sheath, thereby reducing the solvation interaction between water and H^+ (Figure 2h).[37] Quantum chemistry calculations were performed to reap the binding energy of several probable solvation structures of 50M-10S electrolyte. Among these configurations, the $H^+(2H_2O\text{-}1MMZ\text{-}1SO_4^{2-})$ exhibits an interaction energy of −236.37 kJ/mol, which corresponds to the highest absolute value. This suggests that its structure is the most stable, which is basically consistent with the solvation structures obtained from MD simulations (Figure S7 a). Especially, the high interaction energy of MMZ with H^+ indicated that MMZ-H^+ as a whole was energetically favorable to be inserted into/extracted from the electrodes (Figure S7 b).

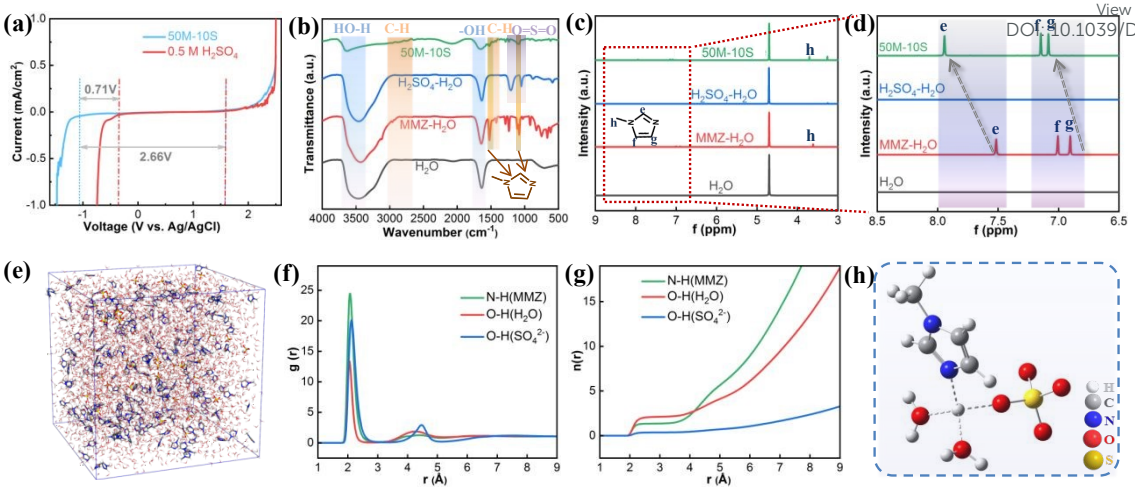

Figure 2. (a) Electrochemical stability window of 50M-10S electrolyte and 0.5 M H_2SO_4 measured by LSV. The FTIR spectra (b) and ^{1}H NMR spectra (c, d) of 50M-10S electrolyte and control groups. (e) Snapshot of MD simulation box of 50M-10S electrolyte. (f) The radial distribution function (RDFs) of the 50M-10S electrolyte for the H-O and H-N. (g) The coordination numbers of H-O and H-N of the 50M-10S electrolyte. (h) Schematic illustration of the H^+ solvation structure in the 50M-10S electrolyte.

Electrochemical performances

The hexaazatrinaphthalene-2, 8, 14-tricarbonitrile (HATN-3CN) was used as a model electrode material to testify the charge storage mechanism in such electrolytes. The ^{1}H-NMR and High-Resolution Mass Spectrometry (HRMS) of the HATN-3CN were displayed in Figure S8 and Figure S9, respectively. The powder X-ray diffraction (PXRD) tests indicate that HATN-3CN had good crystalline properties (Figure S10). The fiber-rod structure of HATN-3CN could be observed in scanning electron microscope (SEM) and transmission electron microscope (TEM) images (Figure S11). The electrochemical performance of HATN-3CN in Swagelok cell was investigated through taking HATN-3CN, activated carbon (AC), and Ag/AgCl as working, counter and reference electrodes, respectively. The Nyquist plots of HATN-3CN electrode showed that the semicircular diameters in those electrolytes were even less than that in pure 0.5 M H_2SO_4 when the molar ratio of MMZ to H_2SO_4 was less than 62.5:10 (Figure 3a, b). It was well illustrated that the addition of a minor amount of MMZ could reduce

View Article Online
DOI: 10.1039/D5SC02677F

the charge transfer resistance between electrolyte and electrode. However, the semicircular diameter increased upon a significant addition of MMZ. This is because the addition of excess MMZ causes an increased viscosity of the electrolyte, and affects the ion transport[38]. Figure 3c and Figure S12 showed the rate performance of HATN-3CN electrode in the electrolytes with different additions of MMZ under the current densities of 0.1-10 A g^{-1}. The electrode in 50M-10S electrolyte exhibited the optimal performance (287.6 mAh g^{-1}, 0.1 A g^{-1}), far better than that in pure 0.5 M H_2SO_4 (206.8 mAh g^{-1}, 0.1 A g^{-1}). According to the principle of solubility similarity, the MMZ ligand of H^+(MMZ) may show stronger affinity to the HATN-3CN molecules than H_2O and thus better wet the electrode, which will facilitate the (de)insertion dynamics of ions. In contrast, when the H_3O^+ ions approach the surface of the material, due to their poor affinity, some ions may experience ineffective collisions, resulting in a decrease in the overall delivery efficiency.[39] The galvanostatic charge-discharge (GCD) curves of HATN-3CN electrode in a series of M-S electrolytes were shown in Figure S13. The rate specific capacities of HATN-3CN electrode were found to increase firstly and then decrease with increasing the MMZ content, with the best result in 50M-10S electrolyte. The cycling performances of HATN-3CN in 0.5 M H_2SO_4 and 50M-10S electrolyte were showed in Figure 3d. The capacity slowly decreased to 263.9 mAh g^{-1} with the 98.8% capacity retention in 50M-10S electrolyte (1 A g^{-1}, 1000 cycles), which was superior to that in 0.5 M H_2SO_4 electrolyte (94.0% capacity retention, 1 A g^{-1}, 1000 cycles). The GCD curves in the 1st, 10th, 100th, 500th and 1000th cycle were exhibited in Figure S14 a and the cycle voltammetry (CV) curve after 1000 cycles was shown in Figure S14 b. Almost constant peak shapes indicated good electrochemical stability of the HATN-3CN electrodes. The obvious fiber-rod structure of HATN-3CN electrodes was clearly visible in the SEM image after 1000 cycles, which also indicated the favorable structural stability of the materials (Figure S15). A series of measurements were carried out to probe into the underlying reasons for the enhanced capacity of HATN-3CN in 50M-10S electrolyte. The CV curves of HATN-3CN electrode were showed in Figure 3e and Figure S16 in several different M-S electrolytes. With growing MMZ molar ratios, the area of the pair of redox peaks on the right side (corresponding

to a higher potential) increased significantly and the potential disparity between the two pairs of redox peaks expanded dramatically. This apparent difference prompted us to hypothesize that a new type of inserted ion (MMZ-H^+) emerges beyond the H^+ due to the addition of MMZ to 0.5 M H_2SO_4. Two sets of experiments were conducted to confirm the availability of MMZ-H^+ insertion. First, we configured the 1 M aqueous solution of 1,3-dimethylimidazolium chloride (1 M DMMZC, pH=8.23) as the electrolyte. The obvious redox peaks for the HATN-3CN electrode could also be observed and a high specific capacity of 191.1 mAh/g (0.1 A g^{-1}) was obtained, indicating that large-sized dimethylimidazolium (DMMZ) ions could be inserted into the HATN-3CN electrode but with obvious polarization (Figure S17 a, b and c). In addition, a 1-methyl-1,2,4-triazole (MTZ)-H_2SO_4 electrolyte (pH=6.52) with a similar pH value to the 50M-10S electrolyte was also configured. The MTZ molecule has a similar size to MMZ but exhibited significantly lower basicity. According to previous reports, only hydrogen ions can insert into or extract from electrodes in the MTZ-acid electrolytes.[17, 40] Under the same test conditions, the profile of CV curve for the HATN-3CN electrode in MTZ-H_2SO_4 electrolyte was similar to that in 0.5 M H_2SO_4, indicating hydrogen ions are the dominant insertion ions in such an electrolyte (Figure S17d). The two sets of experiments prove that large-sized DMMZ ions and small-sized hydrogen ions can both inserted into HATN-3CN electrode but have markedly different reaction dynamics.

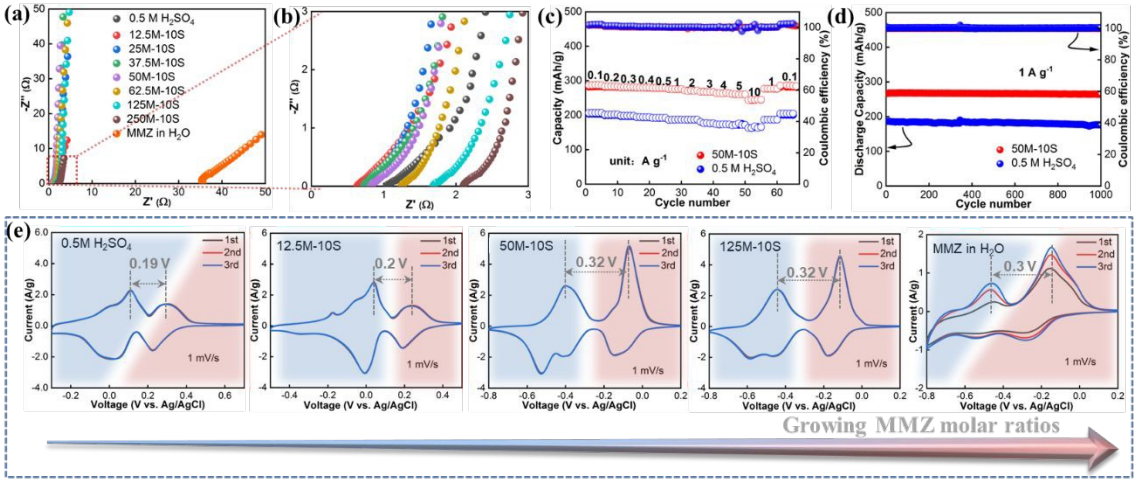

Figure 3. (a, b) Nyquist plots, (c) Rate performance (d) long-term cycling stability, (e) CV curves of HATN-3CN electrode in a series of electrolytes.

View Article Online
DOI: 10.1039/D5SC02677F

Furthermore, a series of characterization methods were performed to verify the assumption that MMZ-H^+ cations might take part in the redox processes. The charge and discharge curves were shown in Figure 4a and different voltage points were selected for ex situ measurements. As shown in Figure 4b, in the ex-situ FT-IR spectra, the intensity of the -C=N- peak (1565 cm^{-1}) weakened during the charge process whereas it was recovered during the opposite process.[41] However, no visible change was observed for the peaks of the –C≡N group. This consequence illustrated that -C=N- groups act as the active centers during the redox process rather than –C≡N groups. The similar result was observed in in-situ Raman spectra (Figure 4c). The peaks located at 1460 cm^{-1} were attributed to the absorption of -C-N- group.[42] The change trend of peak intensity of the -C-N- group was the opposite of -C=N- during the charging and discharging process, which meant a good reversable conversion between the -C=N- and -C-N- groups.

Subsequently, the ex-situ X-ray photoelectron spectra (XPS) were used to explore the characteristics of carbon-nitrogen bonding of HATN-3CN electrode in different voltage states. As shown in Figure 4d, the -C=N-C- peak was dominant at the pristine state. Upon full discharge, the obvious enhancement of -C-N- peak (including -C-N-H peak and -C-N$^-$MMZ-H^+ peak) and the decrease of -C=N-C- peak indicated that HATN-3CN electrode was reduced during the discharge process. With the insertion of MMZ-H^+ cations, an emerging -C-N$^-$MMZ-H^+ peak appeared between -C-N-H peak and –C=N- peak. In addition, due to the electron-withdrawing effect of the proton, a new –C=N-H^+ peak belonging to the protonated MMZ appeared in the position with a higher binding energy than -C=N-C- peak. After full charging, the -C=N-C- peak became dominant again, the -C-N- peak decreased, and the –C=N-H^+ and -C-N$^-$MMZ-H^+ peaks disappeared, indicating the involvement of MMZ-H^+ as a whole in the charging and discharging process. Besides, the peak of –C≡N was almost constant throughout the charging and discharging process.

To further figure out charge storage mechanism of HATN-3CN electrode during charge and discharge, the ex-situ ^{1}H-NMR spectra were conducted. The H chemical

View Article Online
DOI: 10.1039/D5SC02677F

shift values of pure HATN-3CN power and MMZ were first examined for reference. As shown in Figure 4e, the ^{1}H chemical shifts of pure HATN-3CN powder in 9.2, 8.7 and 8.4 ppm were labeled as h, i and j, respectively. Similarly, m (9.03 ppm), n (7.69 ppm), o (7.66 ppm) and p (3.88 ppm) were marked in ^{1}H-NMR spectrum of 1-methylimidazolium ion (Figure 4f). Note that to obtain the ^{1}H chemical shifts of the 1-methylimidazolium ion, we tested a series of M-S solutions with different molar ratios of MMZ to H_2SO_4 (Figure S18). The ^{1}H resonance signal of the 1-methylimidazolium ion exhibited a progressive downfield shift with increasing the molar ratio of H_2SO_4. Once the molar ratio between MMZ and H_2SO_4 reached 1:2, the system attained a state of equilibrium. Subsequent increases in H_2SO_4 content did not significantly change the chemical shift of 1-methylimidazole, confirming full protonation of the imidazole moiety. The invariant δ value was therefore designated as the ^{1}H chemical shifts of the MMZ-H^+ ions. The evolution of ^{1}H-NMR spectra of HATN-3CN electrodes in 50M-10S electrolyte was shown in Figure 4g during charging and discharging. In the initial state, three peaks belonging to HATN-3CN are clearly observed in the spectrum. When the electrode was discharged to -0.25 V, the extra peaks of m, n, o, p, and MMZ-H^+ appeared and the intensities increased gradually with the enhanced discharge depth, indicating that the insertion of MMZ-H^+. The peaks of MMZ-H^+ and H^+ were both observed in the full discharge state. Moreover, the coordinated H^+ of the inserted MMZ-H^+ ions and the inserted H^+ ions in HATN-3CN electrode showed the same integrated area. In view of high practical specific capacity of HATN-3CN electrode (287.6 mAh g^{-1} vs theoretical specific capacity of 350 mAh g^{-1}), 82.2% of the active sites has been utilized, and thus it was thought that in 50M-10S electrolyte, three MMZ-H^+ ions and three H^+ ions could be inserted into one HATN-3CN molecule simultaneously. Conversely, in the charge process, along with the rising of the potential, the peak intensities of of m, n, o, p, MMZ-H^+ and H^+ decreased gradually. When charged to 0.2 V, the peaks of MMZ-H^+ and H^+ both disappeared and HATN-3CN turned back to its initial state. The increased electromagnetic shielding effect from the electron-rich reduced state intermediate of HATN-3CN was responsible for a decrease in the chemical shift values of h, i, and j.[43] The ex situ ^{1}H-NMR spectra of HATN-3CN

electrodes in the 0.5 M H_2SO_4 were showed in Figure S19 as control. In the fully discharged state, only peak of H^+ was observed and it disappeared with charging, suggesting that the HATN-3CN electrodes underwent mainly reversible insertion and extraction of H^+ in the 0.5 M H_2SO_4.

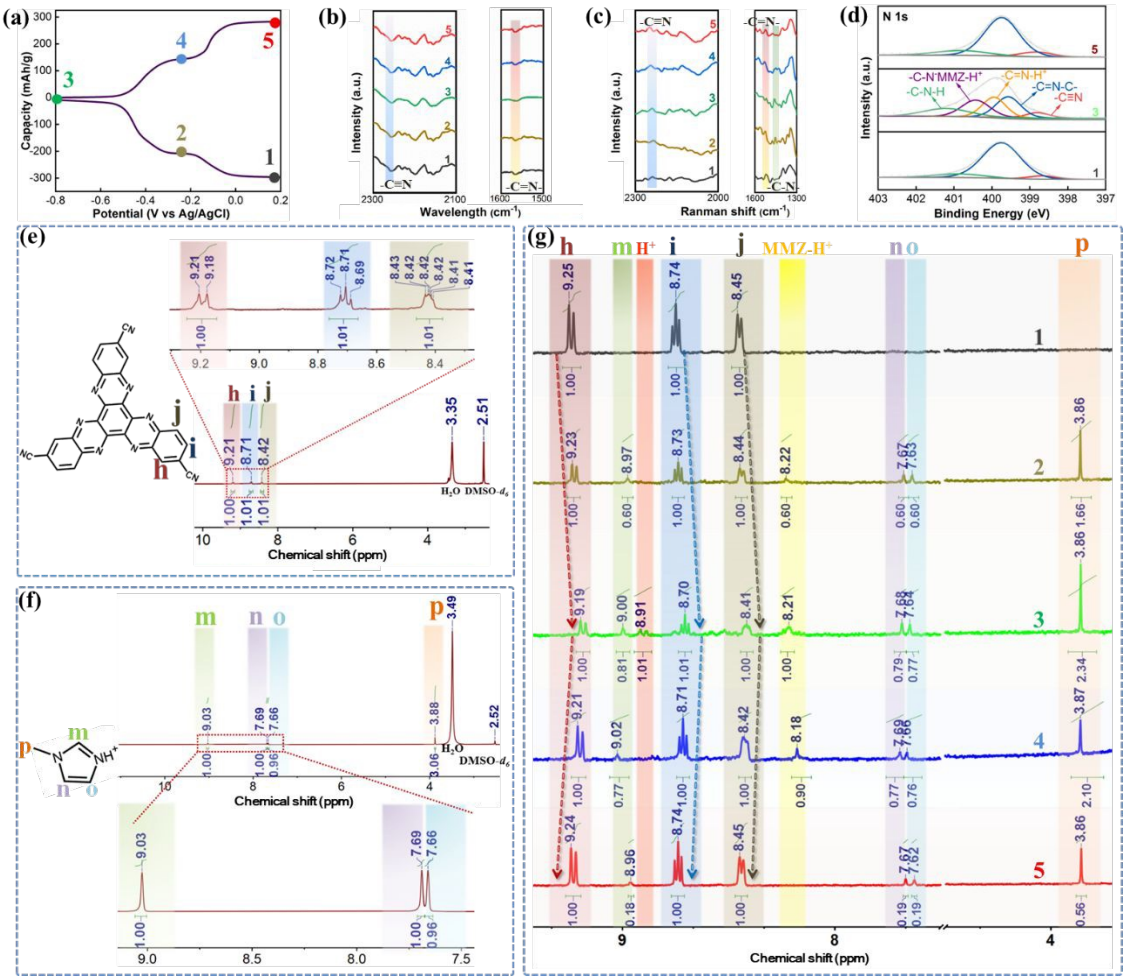

Figure 4. Energy storage mechanism of HATN-3CN in 50M-10S electrolyte. (a) Indication of different charge and discharge states. (b) Ex-situ FT-IR spectra. (c) In-situ Raman spectra. (d) Ex-situ XPS spectra of N 1s. ^{1}H-NMR spectra of pure HATN-3CN powder (e) and imidazolium ion (MMZ/H_2SO_4=1:2) (f). (g) Ex situ ^{1}H-NMR spectra. Note: the solvents used for the ^{1}H-NMR spectra were DMSO-d_6 in e, f and g.

Theoretical calculations based on DFT were used to further comprehend the charge storage process of the HATN-3CN electrode in the 50M-10S and 0.5 M H_2SO_4

View Article Online DOI: 10.1039/D5SC02677F

electrolytes. Due to cyan groups substitution-derived molecular asymmetry, the N active sites of HATN-3CN could be categorized into two groups, named as a and b (Figure S20). The b site had the priority of reaction, based on the adsorption energy calculations. To investigate the type of inserted ions, the energy for the insertion of H^+ derived from the desolvation of MMZ-H^+ and the energy for the insertion of MMZ-H^+ were calculated, respectively (Figure S21). The results showed that the insertion of MMZ-H^+ required lower energy, so the HATN-3CN electrode was dominated by the insertion of MMZ-H^+ at the beginning of the discharge. Then, with MMZ-H^+ occupying all b sites, it was no longer possible to insert MMZ-H^+ due to strong steric hindrance (the structure with two MMZ-H^+ inserted in adjacent N positions cannot be well optimized, Figure S22. Therefore, only small-sized H^+ was allowed to insert into HATN-3CN electrode after three b sites was occupied by MMZ-H^+. Since the molar content of MMZ is much higher than H^+ of 0.5 M H_2SO_4 in 50M-10S electrolyte, the vast majority of H^+ is trapped by MMZ. Thus, the direct insertion of free H^+ in the 50M-10S electrolyte are excluded from consideration and H^+ can only be sourced from MMZ-H^+ desolvation. The ion diffusion process in the HATN-3CN electrode during charging and discharging was further explored using galvanostatic intermittent titration technique (GITT) and EIS. The GITT profiles of HATN-3CN electrode in 50M-10S electrolyte and 0.5 M H_2SO_4 were shown in Figure S23 a. The ion diffusion coefficients of HATN-3CN electrode in 50M-10S electrolyte was high enough (10^{-10}-10^{-9}) compared with other reported aqueous electrolytes with various mass transfer ions, although it was an order of magnitude lower than that in 0.5 M H_2SO_4 (10^{-9}-10^{-8}). The faster transport of H^+ than MMZ-H^+ ions may be due to its smaller size and lower hopping energy barrier in the electrode.[44] From the previous characterizations, it could be seen that both MMZ-H^+ and H^+ were inserted into the HATN-3CN electrode in the 50M-10S electrolyte. If the H^+ is the free H^+ (or hydronium ion) from 50M-10S electrolyte, the ion diffusion coefficients of region 4 corresponding to the (de)insertion of H^+ will be higher than region 3 corresponding to extraction of MMZ-H^+, yet the truth was just the opposite (Figure S23 b). Furthermore, EIS of HATN-3CN at different charge-discharge stages were shown in Figure S24, where region 1 and 4 corresponded

to the (de)bonding of H^+ and the diffusion of MMZ-H^+ in HATN-3CN electrode and region 2 and 3 corresponded to insertion/extraction of MMZ-H^+. Similar charge transfer resistance and ion diffusion resistance were observed in different regions, further suggesting that inserted H^+ is derived from the (de)solvation of MMZ-H^+ rather than free H^+ (or hydronium ion) in 50M-10S electrolyte.

DFT calculation was employed to gain the Gibbs free energy change of ion insertion processes in two paths (Figure 5a). Path 1 calculated the energy change of free H^+ binding to simulate the electrochemical reduction of HATN-3CN electrode in 0.5 M H_2SO_4 electrolyte. Similarly, path 2 modeled the energy change of HATN-3CN during the electrochemical reaction in 50M-10S electrolyte. Normally, the more negative the Gibbs free energy, the more probable the reaction is to proceed spontaneously.[45] It was clear that the Gibbs free energies for the last three steps barely changed in path 1, while in path 2 they were significantly reduced, suggesting that it was more likely to realize a six-electron reaction through path 2.[46] The molecular electrostatic potential (MESP) was adopted to identify the electrophilic and nucleophilic reaction-active sites (Figure S25).[47] As shown in Figure 5b, N-atoms of initial HATN-3CN with negative MESP values (the blue region) exhibited higher electronegativity, and were attractive for electrophilic cations (MMZ-H^+ or H^+). However, during the ensuing electrochemical reaction, the MESP results in the two reaction paths are not identical. In Figure 5c, due to the electron-deficient nature of the H^+, when the insertion of one H^+ into the N sites of HATN-3CN, the nucleophilicity of the neighboring N sites decreased, resulting in a lower reactivity of the unreacted N sites. However, in Figure 5d, the electron cloud density of the unreacted N active sites of HATN-3CN was significantly higher than that with the insertion of three H^+ because of the stronger electron-donating ability of nitrogen anions combining with MMZ-H^+ cations. This explains the almost unchanged Gibbs free energy in last three steps of path 1, and a significant decrease in Gibbs free energy in path 2 in Figure 5a. Given the above results, both theory and practice have demonstrated that the involvement of MMZ-H^+ enhances the utilization of the active sites of HATN-3CN electrodes and thus boosts the capacity.

View Article Online
DOI: 10.1039/D5SC02677F

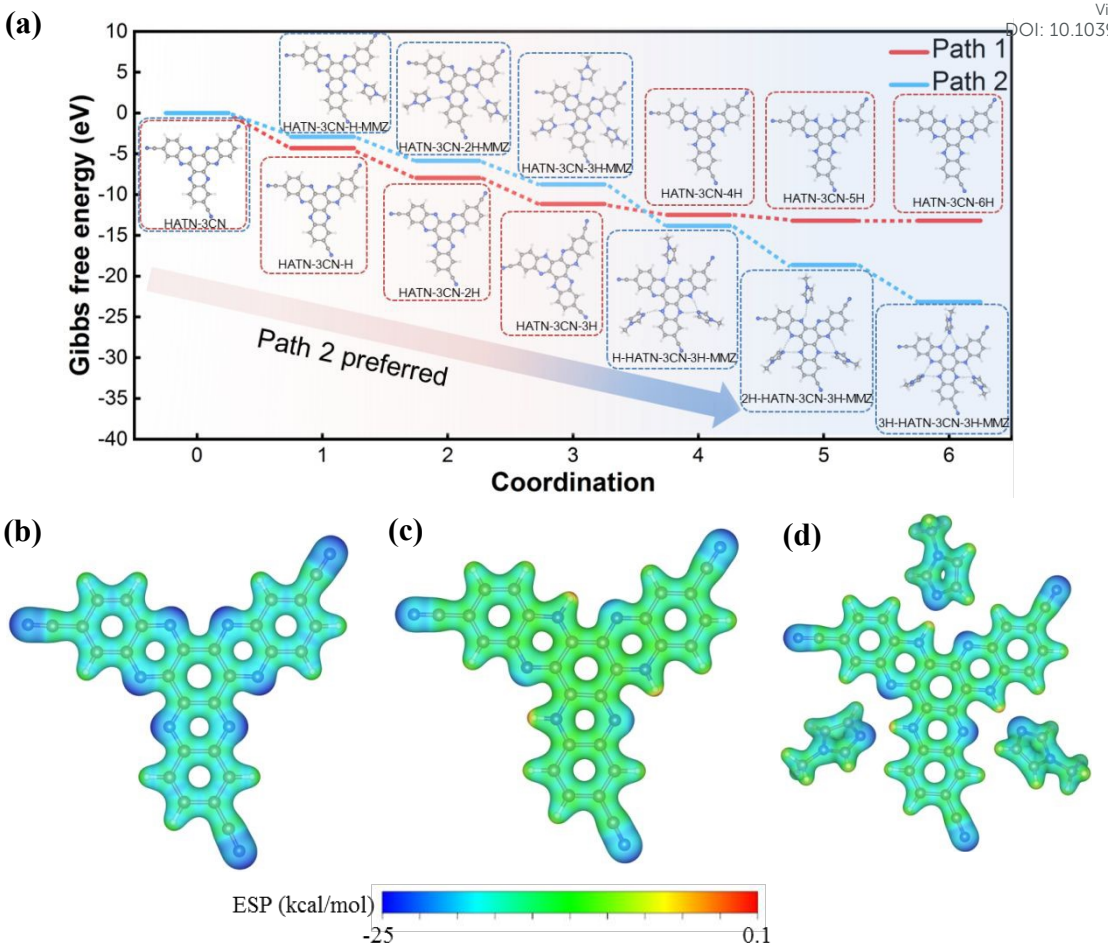

Figure 5. (a) The Gibbs free energy change at each coordination stage with different ions. Calculation of MESP distribution of (b) HATN-3CN, (c) HATN-3CN-3H$^+$ and (d) HATN-3CN-3MMZ-H$^+$.

Electrochemical Performance of the Full Cells

Based on the above results, it has been confirmed that the insertion of MMZ-H$^+$ could enhance the capacity of the HATN-3CN electrode; however, the performance of full cell remains to be explored. MnO_2, which is cost-effective and easy to synthesize, is selected as the cathode. The ε-MnO_2 was synthesized by electrodeposition and evaluated by XRD pattern (Figure S26 a). The SEM images and the energy dispersive spectrometry (EDS) elemental mapping were shown in Figure S26 b. It can be seen that MnO_2 is uniformly deposited on the surface of the carbon fibers with a homogeneous elemental distribution. The charge-discharge curve of the manganese dioxide electrode revealed a distinct discharge plateau (Figure S27 a). It indicates that in our proposed

View Article Online
DOI: 10.1039/D5SC02677F

near-neutral electrolyte MnO_2 can show good electrochemical activity. XPS was used to analyze valence characters of MnO_2 electrode during the charging and discharge process (Figure S27 b). The Mn^{2+} was dominant in Mn 2p spin-orbit peaks after full discharge, which illustrated that a two-electron transfer of manganese was the dominant reaction[48]. The CV curves of MnO_2 electrode were shown in Figure S27 c. The redox potential of MnO_2 electrode in the 0.5 M $MnSO_4$+50M-10S electrolyte was lower than that in H_2SO_4 electrolyte, which was similar to that in $Mn(Ac)_2$ electrolyte.[49] Specifically, the reduced electrode potential of MnO_2/Mn^{2+} was related to low H^+ concentration and the reduced Gibbs free energy change. Because the Gibbs free energy of MMZ-H^+ was lower than that of free H^+ in H_2SO_4, less energy was required to accomplish the reaction (Equation 1), and therefore the electrode potential of MnO_2/Mn^{2+} in 50M-10S electrolyte was decreased.

Next, a full cell was assembled by using HATN-3CN as the anode, MnO_2 as the cathode and 0.5 M $MnSO_4$ + 50M-10S as the electrolyte. Considering the near-neutral electrolyte, H^+ and OH^- were avoided to appear in the electrochemical equations. Schematic illustration of full battery was shown in Figure 6a, during charging, Mn^{2+} was oxidized into MnO_2 accompanied by the formation of MMZ-H^+ (Equation 1). Simultaneously, in the anode, MMZ-H^+ in the electrolyte were inserted to HATN-3CN (Equation 2). Then H^+ formed by MMZ-H^+ desolvation were inserted into the electrode (Equation 3). The process was reversed during discharging process.

$$3Mn^{2+} + 12\text{MMZ} + 6\text{H}_2\text{O} \leftrightarrow 3MnO_2 + 12\text{MMZ-H}^+ + 6e^- \quad 1$$

$$\text{HATN-3CN} + 3\text{MMZ-H}^+ + 3e^- \leftrightarrow \text{HATN-3CN-3H-MMZ} \quad 2$$

$$\text{HATN-3CN-3H-MMZ} + 3\text{MMZ-H}^+ + 3e^- \leftrightarrow \text{3H-HATN-3CN-3H-MMZ} + 3\text{MMZ} \quad 3$$

The CV curves of the HATN-3CN//MnO_2 full cell was tested in a potential window of 0-1.2 V, and the obvious reduction and oxidation peaks manifested that the predicted redox reactions have occurred (Figure 6b). The rate performance of HATN-3CN//MnO_2 was systematically evaluated at various current densities (Figure 6c). The full battery had a high specific capacity of 266.2 mA h g^{-1} at 1 A g^{-1} (based on the anode mass). Even at a high current density of 10 A g^{-1}, the capacity still remained at

185.8 mA h g^{-1}. When the current density returned to 1 A g^{-1}, the specific capacity recovered to its initial value. These results clearly indicated that the HATN-3CN//MnO_2 battery has fast ion transfer capability and good reversibility. The charge-discharge curves of the HATN-3CN//MnO_2 full cell at various current densities were shown in Figure 6d, and the results are consistent with those of the CV profiles. Figure 6e showed the long cycle performance of HATN-3CN//MnO_2 full cell in 0.5 M $MnSO_4$+50M-10S electrolyte. The capacity of the full cell decayed very slowly in 0.5 M $MnSO_4$ + 50M-10S electrolyte during the cycles, and 97 % capacity retention was observed after 1000 cycles at 1 A g^{-1}. In addition, the coulombic efficiency of the full cell remained at around 100% during the 1000 cycles in 0.5 M $MnSO_4$+50M-10S electrolyte. That electrochemical performance is excellent compared to most reported aqueous ion batteries (Table S5). The charge-discharge curves during the 1st, 10th, 100th, 500th, and 1000th cycles of the full cell were shown in Figure S28 in 0.5 M $MnSO_4$+50M-10S electrolyte, and the platform of curves were distinct and essentially remained unchanged, indicating an excellent cycling stability. The digital image of battery cases after 1000 cycles in 0.5 M $MnSO_4$ + 50M-10S electrolyte was displayed in Figure S29, which remained bright and flat after cycling. Figure S30 presented the digital images of coin cell components after being soaked in the 50M-10S electrolyte for 2 h. Notably, the color of 0.5 M H_2SO_4 solution changed from transparent to shallow green while that of 50M-10S electrolyte remained unchanged. The above results indicate that the addition of a small amount of MMZ to the sulfuric acid can reduce the corrosion of the electrolyte on metallic components of button batteries, thus enhancing the compatibility of proton batteries with conventional metal package technology. The HATN-3CN//MnO_2 full cell had high energy density of 128.0 Wh kg^{-1} at the power density of 480 W kg^{-1} and could light light-emitting diode (LED) screen at 25 $^{\circ}$C (Figure 6f). The HATN-3CN//MnO_2 pouch cell with high active substance loading still had a high specific capacity of 208.4 mA h g^{-1} at 1 A g^{-1} (based on the anode mass) (Figure 6g). The CV and GCD curves were similar to button cell batteries (Figure S31). The pouch cell could light light-emitting diode (LED) screen after curling and folding (Figure 6h), indicating the good application potential of 50M-10S electrolyte in aqueous

View Article Online
DOI: 10.1039/D5SC02677F

imidazolium-ion battery. In brief, the cell with the near-neutral pH imidazolyl electrolyte exhibits attractive electrochemical properties and promising applications.

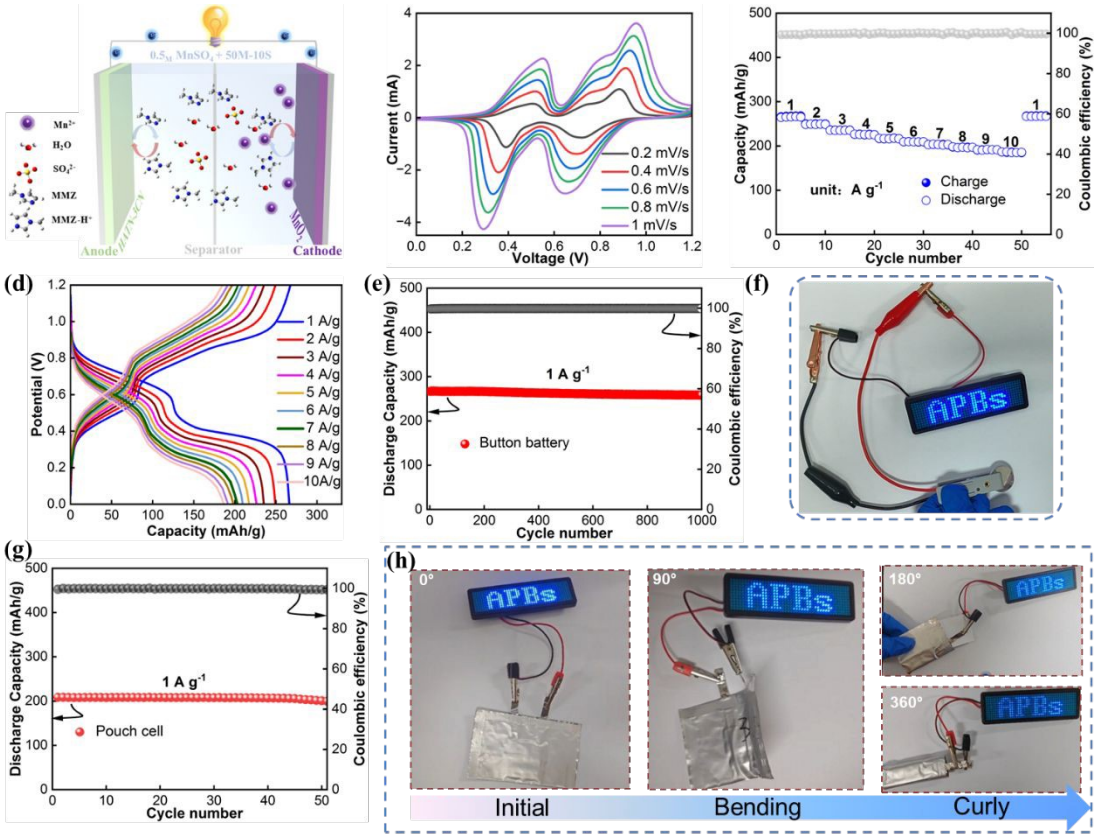

Figure 6. Electrochemical performance of HATN-3CN//MnO_2 full battery. (a) Schematic illustration of full battery. (b) CV curves at different scan rates from 0.2 to 1 mV/s, (c) Rate performance, (d) Charge-discharge curves, (e) Cycling performance at 1 A g^{-1} and (f) Optical image of an LED screen powered by button-type battery. (g) Cycling performance at 1 A g^{-1} and (h) Optical image of an LED screen powered of pouch cell.

Conclusion

In this work, we first reported the aqueous imidazolium-ion battery with MMZ-H^+/H^+ dual charge carriers. Due to the insertion of MMZ-H^+, the utilization efficiency of the active site of HATN-3CN electrode was enhanced. The capacity has been increased by 40% compared to pure H^+ transfer (287.6 mAh g^{-1} in 50M-10S electrolyte vs. 206.8 mAh g^{-1} in 0.5 M H_2SO_4 electrolyte, 0.1 A g^{-1}), which is comparable or

superior to classic aqueous metal ion batteries, such as Zn^{2+}, Na^{+} and K^{+} batteries, not to mention the rate performance.[46, 50, 51] The assembled MnO_2//HATN-3CN full batteries with MMZ-based neutral electrolyte show superior capacity and stability. These results will shed light on the study of novel electrolyte with low corrosion, wide voltage window and high ionic conductivity for aqueous batteries as well as opening an avenue for the development of sustainable batteries that do not rely on metal ions as charge carriers. More interestingly, the insertion and extraction of such large-size MMZ-H^{+} cations in organic electrode materials may bring new opportunities for intercalation chemistry, the preparation of organic 2D materials, and development of new-type ion batteries.

Data availability

The data supporting this article have been included as part of the ESI.

Author Contributions

Conceptualization, M. J. H. and J. Y.; Writing – original draft, H. P. Y.; Writing – review & editing, M. J. H. and J. Y.; Investigation, H. P. Y., R. L., Z. H. W., B. W., M. X. L., G. Q. Z., X. Y. W., X. R. Y., Y. X. H., H. G. M., and J. R. L.; Formal analysis, H. P. Y.; Funding acquisition, M. J. H. and J. Y.; All authors did a final check and approved the final version for submission.

Acknowledgements

We acknowledge the financial support by the National Natural Science Foundation of China (22371010, 21771017 and 51702009), the "Hundred Talents Program" of the Chinese Academy of Science, Fundamental Research Funds for the Central Universities, Shenzhen Science and Technology Program (JCYJ20210324115412035 JCYJ2021-0324123202008, JCYJ20210324122803009 and ZDSYS20210813095534001), Guangdong Basic and Applied Basic Research

View Article Online
DOI: 10.1039/D5SC02677F

Foundation (2021A1515110880).

Competing interests

The authors declare no conflict of interest.

References

1. Z. Yang, J. Zhang, M. C. W. Kintner-Meyer, X. Lu, D. Choi, J. P. Lemmon and J. Liu, Electrochemical Energy Storage for Green Grid, *Chem. Rev.*, 2011, **111**, 3577-3613.
2. L. E. Blanc, D. Kundu and L. F. Nazar, Scientific Challenges for the Implementation of Zn-Ion Batteries, *Joule*, 2020, **4**, 771-799.
3. M. Li, J. Lu, Z. Chen and K. Amine, 30 Years of Lithium-Ion Batteries, *Adv. Mater.*, 2018, **30**, 1800561.
4. S. Wang, J. Shi, Z. Liu and Y. Xia, Advanced Ether-Based Electrolytes for Lithium-ion Batteries, *Adv. Energy Mater.*, 2024, **14**, 2401526.
5. Z. Wang, R. Li, G. Zhao, X. Yan, X. Wang, H. Yu, Y. Hao, Y. Dai, H. Ma, M. Li, H. Li, M. Yang, B. Wang, J. Liu, M. Hu and Y. Jun, External ligand-free nickel-catalyzed synthesis of polypyrazines towards stable, high-capacity and low-potential sodium ion storage, *Chem. Eng. J.*, 2024, **499**, 155900.
6. Z. Guo, J. Huang, X. Dong, Y. Xia, L. Yan, Z. Wang and Y. Wang, An organic/inorganic electrode-based hydronium-ion battery, *Nat. Commun.*, 2020, **11**, 959.
7. Q. Liu, Z. Hu, W. Li, C. Zou, H. Jin, S. Wang, S. Chou and S.-X. Dou, Sodium transition metal oxides: the preferred cathode choice for future sodium-ion batteries?, *Energy Environ. Sci.*, 2021, **14**, 158-179.
8. W. Zhang, Y. Liu and Z. Guo, Approaching high-performance potassium-ion batteries via advanced design strategies and engineering, *Sci. Adv.*, **5**, eaav7412.
9. D. Kundu, B. D. Adams, V. Duffort, S. H. Vajargah and L. F. Nazar, A high-capacity and long-life aqueous rechargeable zinc battery using a metal oxide intercalation cathode, *Nat. Energy*, 2016, **1**, 16119.

10. H. Zhang, Y. Tian, W. Wang, Z. Jian and W. Chen, Organic Ammonium Ion Battery: A New Strategy for a Nonmetallic Ion Energy Storage System, *Angew. Chem. Int. Ed.*, 2022, **61**, e202204351.

11. H. Guo, L. Wan, J. Tang, S. Wu, Z. Su, N. Sharma, Y. Fang, Z. Liu and C. Zhao, Stable colloid-in-acid electrolytes for long life proton batteries, *Nano Energy*, 2022, **102**, 107642.

12. R. Li, M. Yang, H. Ma, X. Wang, H. Yu, M. Li, Z. Wang, L. Zheng, H. Li, Y. Hao, M. Hu and J. Yang, A Natural Casein-Based Separator with Brick-and-Mortar Structure for Stable, High-Rate Proton Batteries, *Adv. Mater.*, 2024, **36**, 2403489.

13. M. Yang, Q. Zhao, H. Ma, R. Li, Y. Wang, R. Zhou, J. Liu, X. Wang, Y. Hao, J. Ren, Z. Zheng, N. Zhang, M. Hu, J. Luo and J. Yang, Integrated Uniformly Microporous C4N/Multi-Walled Carbon Nanotubes Composite Toward Ultra-Stable and Ultralow-Temperature Proton Batteries, *Small*, 2023, **19**, 2207487.

14. G. Zhao, X. Yan, Y. Dai, J. Xiong, Q. Zhao, X. Wang, H. Yu, J. Gao, N. Zhang, M. Hu and J. Yang, Searching High-Potential Dihydroxynaphthalene Cathode for Rocking-Chair All-Organic Aqueous Proton Batteries, *Small*, 2024, **20**, 2306071.

15. X. Wu, Y. Qi, J. J. Hong, Z. Li, A. S. Hernandez and X. Ji, Rocking-Chair Ammonium-Ion Battery: A Highly Reversible Aqueous Energy Storage System, *Angew. Chem. Int. Ed.*, 2017, **56**, 13026-13030.

16. A. Kulkarni, C. Padwal, J. MacLeod, P. Sonar, T. Kim and D. Dubal, Toward Safe and Reliable Aqueous Ammonium Ion Energy Storage Systems, *Adv. Energy Mater.*, 2024, **14**, 2400702.

17. H. Ma, M. Yang, R. Li, Y. Wang, L. Zheng, X. Jing, Y. Hao, Y. Dai, J. Gao, M. Hu and J. Yang, An organic acid-alkali coordinately regulated liquid electrolyte enables stable cycling of high-voltage proton battery, *Chem. Eng. J.*, 2024, **486**, 150102.

18. Y. Xu, X. Wu, H. Jiang, L. Tang, K. Y. Koga, C. Fang, J. Lu and X. Ji, A Non-aqueous H3PO4 Electrolyte Enables Stable Cycling of Proton Electrodes, *Angew. Chem. Int. Ed.*, 2020, **59**, 22007-22011.

19. Y. Hao, M. Yang, H. Ma, R. Li, X. Jing, X. Wang, H. Yu, Y. Dai, M. Li, Z. Wang, H. Li, X. Yan, G. Zhao, B. Wang, J. Liu, M. Hu and J. Yang, Natural low corrosive phytic acid electrolytes enable green, ultrafast, stable and high-voltage aqueous proton battery, *Energy*

View Article Online
DOI: 10.1039/D5SC02677F

Storage Mater., 2024, **70**, 103455.

20. M. Liao, X. Ji, Y. Cao, J. Xu, X. Qiu, Y. Xie, F. Wang, C. Wang and Y. Xia, Solvent-free protic liquid enabling batteries operation at an ultra-wide temperature range, *Nat. Commun.*, 2022, **13**, 6064.
21. Y. Wang, T. Wang, S. Bu, J. Zhu, Y. Wang, R. Zhang, H. Hong, W. Zhang, J. Fan and C. Zhi, Sulfolane-containing aqueous electrolyte solutions for producing efficient ampere-hour-level zinc metal battery pouch cells, *Nat. Commun.*, 2023, **14**, 1828.
22. B. Su, J. Deng, Z. Wu, X. Li, J. Li, H. Yu, P. Li, H. Li, L. Yan, L. Zhang, T.-F. Yi, T. Ma and J. Shu, Water-in-Acid Strategy for Corrosion-Free Proton Storage: Phosphoric Acid Electrolyte Engineering Toward Sustainable Aqueous Batteries, *Angew. Chem. Int. Ed.*, 2025, **n/a**, e202505769.
23. M. Liao, Y. Cao, Z. Li, J. Xu, Y. Qi, Y. Xie, Y. Peng, Y. Wang, F. Wang and Y. Xia, VPO4F Fluorophosphates Polyanion Cathodes for High-Voltage Proton Storage, *Angew. Chem. Int. Ed.*, 2022, **61**, e202206635.
24. X. Tang, S. Lv, K. Jiang, G. Zhou and X. Liu, Recent development of ionic liquid-based electrolytes in lithium-ion batteries, *J. Power Sources*, 2022, **542**, 231792.
25. C. Karlsson, C. Strietzel, H. Huang, M. Sjödin and P. Jannasch, Nonstoichiometric Triazolium Protic Ionic Liquids for All-Organic Batteries, *ACS Appl. Energy Mater.*, 2018, **1**, 6451-6462.
26. M. Armand, F. Endres, D. R. MacFarlane, H. Ohno and B. Scrosati, Ionic-liquid materials for the electrochemical challenges of the future, *Nat. Mater.*, 2009, **8**, 621-629.
27. Q. Zhao, S. Stalin and L. A. Archer, Stabilizing metal battery anodes through the design of solid electrolyte interphases, *Joule*, 2021, **5**, 1119-1142.
28. P. Liang, S. Di, Y. Zhu, Z. Li, S. Wang and L. Li, Realization of Long-Life Proton Battery by Layer Intercalatable Electrolyte, *Angew. Chem. Int. Ed.*, 2024, **63**, e202409871.
29. L. Zhao, Y. Li, M. Yu, Y. Peng and F. Ran, Electrolyte-Wettability Issues and Challenges of Electrode Materials in Electrochemical Energy Storage, Energy Conversion, and Beyond, *Adv. Sci.*, 2023, **10**, 2300283.
30. C. Karlsson and P. Jannasch, Highly Conductive Nonstoichiometric Protic Poly(ionic liquid) Electrolytes, *ACS Appl. Energy Mater.*, 2019, **2**, 6841-6850.

31. S. Wu, J. Chen, Z. Su, H. Guo, T. Zhao, C. Jia, J. Stansby, J. Tang, A. Rawal, Y. Pang, J. Ho and C. Zhao, Molecular Crowding Electrolytes for Stable Proton Batteries, *Small*, 2022, **18**, 2202992.

32. M. Zhang, H. Hua, P. Dai, Z. He, L. Han, P. Tang, J. Yang, P. Lin, Y. Zhang, D. Zhan, J. Chen, Y. Qiao, C. C. Li, J. Zhao and Y. Yang, Dynamically Interfacial pH-Buffering Effect Enabled by N-Methylimidazole Molecules as Spontaneous Proton Pumps toward Highly Reversible Zinc-Metal Anodes, *Adv. Mater.*, 2023, **35**, 2208630.

33. H. Wang, R. Emanuelsson, C. Karlsson, P. Jannasch, M. Strømme and M. Sjödin, Rocking-Chair Proton Batteries with Conducting Redox Polymer Active Materials and Protic Ionic Liquid Electrolytes, *ACS Appl. Mater. Interfaces*, 2021, **13**, 19099-19108.

34. R. Wang, Q. Ma, L. Zhang, Z. Liu, J. Wan, J. Mao, H. Li, S. Zhang, J. Hao, L. Zhang and C. Zhang, An Aqueous Electrolyte Regulator for Highly Stable Zinc Anode Under −35 to 65 °C, *Adv. Energy Mater.*, 2023, **13**, 2302543.

35. T. Yamada and M. Mizuno, Infrared Spectroscopy in the Middle Frequency Range for Various Imidazolium Ionic Liquids—Common Spectroscopic Characteristics of Vibrational Modes with In-Plane +C(2)–H and +C(4,5)–H Bending Motions and Peak Splitting Behavior Due to Local Symmetry Breaking of Vibrational Modes of the Tetrafluoroborate Anion, *ACS Omega*, 2021, **6**, 1709-1717.

36. Y. Shang, S. Chen, N. Chen, Y. Li, J. Lai, Y. Ma, J. Chen, F. Wu and R. Chen, A universal strategy for high-voltage aqueous batteries via lone pair electrons as the hydrogen bond-breaker, *Energy Environ. Sci.*, 2022, **15**, 2653-2663.

37. J. Hao, L. Yuan, C. Ye, D. Chao, K. Davey, Z. Guo and S.-Z. Qiao, Boosting Zinc Electrode Reversibility in Aqueous Electrolytes by Using Low-Cost Antisolvents, *Angew. Chem. Int. Ed.*, 2021, **60**, 7366-7375.

38. H. Tu, Z. Wang, J. Xue, Z. Tang, Y. Liu, X. Liu, L. Liu, S. Lu, S. Weng, Y. Gao, G. Sun, Z. Liu, K. Peng, X. Zhang, D. Li, G. Wu, M. Liu, J. Hu, H. Li, J. Xu and X. Wu, Regulating Non-Equilibrium Solvation Structure in Locally Concentrated Ionic Liquid Electrolytes for Wide-Temperature and High-Voltage Lithium Metal Batteries, *Angew. Chem. Int. Ed.*, 2024, **n/a**, e202412896.

39. Z. Song, L. Wang, W. Jiang, M. Pei, B. Li, R. Mao, S. Liu, T. Zhang, X. Jian and F. Hu,

"Like Compatible Like" Strategy Designing Strong Cathode-Electrolyte Interface Quasi-Solid-State Lithium–Sulfur Batteries, *Adv. Energy Mater.*, 2024, **14**, 2302688.

40. H. Ma, M. Yang, R. Li, L. Zheng, Y. Hao, H. Li, M. Li, G. Zhao, Z. Wang, B. Wang, M. Hu and J. Yang, An Organic Acid-Alkali Coregulated Ionic Liquid Electrolyte Enabling Wide-Temperature-Range Proton Battery, *Small*, 2024, **n/a**, 2405004.

41. Z. Ye, S. Xie, Z. Cao, L. Wang, D. Xu, H. Zhang, J. Matz, P. Dong, H. Fang, J. Shen and M. Ye, High-rate aqueous zinc-organic battery achieved by lowering HOMO/LUMO of organic cathode, *Energy Storage Mater.*, 2021, **37**, 378-386.

42. M. Shi, J. He, Y. Zhao, L. Zhao, K. Dai and C. Yan, In-situ Raman investigation and application of phenazine-based organic electrode in aqueous proton batteries, *Mater. Des.*, 2022, **222**, 111043.

43. X. Song, Y. Ge, H. Xu, S. Bao, L. Wang, X. Xue, Q. Yu, Y. Xing, Z. Wu, K. Xie, T. Zhu, P. Zhang, Y. Liu, Z. Wang, Z. Tie, J. Ma and Z. Jin, Ternary Eutectic Electrolyte-Assisted Formation and Dynamic Breathing Effect of the Solid-Electrolyte Interphase for High-Stability Aqueous Magnesium-Ion Full Batteries, *Journal of the American Chemical Society*, 2024, **146**, 7018-7028.

44. W. Sun, F. Wang, S. Hou, C. Yang, X. Fan, Z. Ma, T. Gao, F. Han, R. Hu, M. Zhu and C. Wang, Zn/MnO2 Battery Chemistry With H+ and Zn2+ Coinsertion, *Journal of the American Chemical Society*, 2017, **139**, 9775-9778.

45. C. Wu, X. Yan, H. Yu, T. Li, J. Xiong, Y. Dai, Q. Guo, J. Liu, G. Shan, M. Hu and J. Yang, Engineering strong electronegative nitrogen-rich porous organic polymer for practical durable lithium-sulfur battery, *J. Power Sources*, 2022, **551**, 232212.

46. Y. Lin, H. Cui, C. Liu, R. Li, S. Wang, G. Qu, Z. Wei, Y. Yang, Y. Wang, Z. Tang, H. Li, H. Zhang, C. Zhi and H. Lv, Inside Back Cover: A Covalent Organic Framework as a Long-life and High-Rate Anode Suitable for Both Aqueous Acidic and Alkaline Batteries (Angew. Chem. Int. Ed. 14/2023), *Angew. Chem. Int. Ed.*, 2023, **62**, e202302702.

47. Q. Zhao, W. Huang, Z. Luo, L. Liu, Y. Lu, Y. Li, L. Li, J. Hu, H. Ma and J. Chen, High-capacity aqueous zinc batteries using sustainable quinone electrodes, *Sci. Adv.*, **4**, eaao1761.

48. Z.-H. Huang, Y. Song, D.-Y. Feng, Z. Sun, X. Sun and X.-X. Liu, High Mass Loading MnO2 with Hierarchical Nanostructures for Supercapacitors, *ACS Nano*, 2018, **12**, 3557-

View Article Online
DOI: 10.1039/D5SC02677F

3567.

49. C. Xie, T. Li, C. Deng, Y. Song, H. Zhang and X. Li, A highly reversible neutral zinc/manganese battery for stationary energy storage, *Energy Environ. Sci.*, 2020, **13**, 135-143.

50. S. Wu, H. Guo, Z. Su, C. Jia, X. Zhang, S. Wang, T. Zhao, Q. Meyer and C. Zhao, Suppressed Manganese Oxides Shuttling in Acidic Electrolytes Extends Shelf-Life of Electrolytic Proton Batteries, *Adv. Funct. Mater.*, 2024, **34**, 2315706.

51. Y. Liang, Y. Jing, S. Gheytani, K.-Y. Lee, P. Liu, A. Facchetti and Y. Yao, Universal quinone electrodes for long cycle life aqueous rechargeable batteries, *Nat. Mater.*, 2017, **16**, 841-848.

View Article Online
DOI: 10.1039/D5SC02677F

Data availability

The data supporting this article have been included as part of the ESI.

View Article Online
DOI: 10.1039/D5SC02677F

Supporting information

High-capacity aqueous imidazolium-ion battery enabled by MMZ-H^+/H^+ co-intercalation in a near neutral electrolyte

Haiping Yu,[a,b] Rui Li,[a,b] Zhihui Wang,[c] Bei Wang,[a,b] Mengxiao Li,[c] Guoqing Zhao,[c] Xinyu Wang,[a,b] Xiaorong Yan,[c] Yuxin Hao,[a,b] Huige Ma,[a,b] Jingru Liu,[a,b] Mingjun Hu,[,c] Jun Yang[*,a,d]*

a Beijing Institute of Nanoenergy & Nanosystems, Chinese Academy of Sciences, Beijing, 101400, China.

b School of Nanoscience and Engineering, University of Chinese Academy of Sciences, Beijing,101408, China.

c School of Materials Science and Engineering, Beihang University, Beijing 100191, China.

d Shenzhen Institute for Advanced Study, University of Electronic Science and Technology of China, Shenzhen, 518000, China.

*Corresponding author, E-mail: mingjunhu@buaa.edu.cn, yangjun@binn.cas.cn.

View Article Online
DOI: 10.1039/D5SC02677F

1. Materials and Methods

1.1 Materials

Triquinoyl hydrate (99%) was purchased from Bidepharm. 3,4-Diaminobenzonitrile (97%), 1,3-Dimethylimidazolium chloride (98%) and 1-methylimidazole (99%) were obtained from Macklin. Manganese sulphate (98%) and 1-methyl-1,2,4-triazole (98%) were purchased by Aladdin. Sulfuric acid (98%) was purchased from TCI Chemicals. Glass fiber separator (GF/A, 4.7 cm) was obtained from Whatman. Ketjen black, activated carbon and polyvinylidene difluoride (PVDF) were purchased from Canrd Technology Co. Ltd. All the solvents were purchased from Aladdin and used as received without further purification.

1.2 General methods

1H nuclear magnetic resonance (NMR) spectra were tested on a Bruker AVANCE IIIHD500 (Bruker, Germany). Powder X-ray diffraction (PXRD) were recorded on a Xpert3 Powder (PANalytical, Holland) with Cu Kα radiation (λ = 1.5418Å). High resolution mass spectra (HRMS) were recorded with a LCMS-IT-TOF (Shimadzu, Japan). Fourier transform infrared (FT-IR) spectra were performed on a Bruker VERTEX80v (Bruker, Germany). Raman spectra were collected at Horiba LabRAM HR Evolution (HORIBA Scientific, Japan) with a laser wavelength of 532 nm. The scanning electron microscopy (SEM) characterizations were performed on a ZEISS Sigma 300 (ZEISS, Germany). Transmission electron microscope (TEM) measurements were conducted using a JEM-F200 (JEOL, Japan). X-ray photoelectron spectroscopy (XPS) measurements were performed on a Fisher Scientific ESCALAB Xi (Thermo, USA), The viscosities were performed on a Rheometer MCR 302 (Anton Paar, Austria).

1.3 Molecular dynamics (MD) simulations

Quantum chemistry calculations were first performed to optimize molecular geometries of MMZ solvent molecule using the Gaussian 16 package[1] at B3LYP/6-311+G(d) level of theory. The atomic partial charges on these solvent molecules were computed by fitting to the molecular electrostatic potential at atomic centers with the Møller-Plesset second-order perturbation method and the correlation-consistent

View Article Online
DOI: 10.1039/D5SC02677F

polarized valence cc-pVTZ(-f) basis set. The atomistic force field parameters for all ions and molecules are described by the AMBER format and are taken from previous work.[2] The cross-interaction parameters between different atom types are obtained from the Lorentz-Berthelot combination rule.

A modelling system consisting of 40 H_2SO_4 ion pairs, 200 MMZ, and 4320 water molecules was constructed. The SPC/E water model was adopted in the current work. Atomistic simulations of this modelling system were performed using GROMACS package with cubic periodic boundary conditions.[3] The equations for the motion of all atoms were integrated using a classic Verlet leapfrog integration algorithm with a time step of 1.0 fs. A cutoff radius of 1.5 nm was set for short-range van der Waals interactions and real-space electrostatic interactions. The particle-mesh Ewald (PME) summation method with an interpolation order of 5 and a Fourier grid spacing of 0.12 nm was employed to handle long range electrostatic interactions in reciprocal space. All simulation systems were first energetically minimized using a steepest descent algorithm, and thereafter annealed gradually from 600 K to 300 K within 5 ns. All annealed simulation systems were equilibrated in an isothermal-isobaric (NPT) ensemble for 10 ns of physical time maintained using a Nosé-Hoover thermostat and a Parrinello-Rahman barostat with time coupling constants of 0.5 and 0.3 ps, respectively, to control the temperature at 300 K, and the pressure at 1 atm. Atomistic simulations were further performed in a canonical ensemble (NVT) for 40 ns, and simulation trajectories were recorded at an interval of 100 fs for further structural and dynamical analysis, and to extract representative solvation structures.

1.4 Density functional theory (DFT) calculations

Density functional theory (DFT) calculations were carried out using Vienna Ab-initio Simulation Package (VASP).[4] The whole system contains a complete graphical interface for setting up, running and analyzing VASP calculations. The projected augmented wave (PAW) potential was employed to describe the core electrons, and the calculations were performed within the framework of the generalized gradient approximation (GGA), specifically using the Perdew-Burke-Ernzerh (PBE) functional to calculate the exchange-correlation energy. [5] The plane wave basis set was extended

View Article Online
DOI: 10.1039/D5SC02677F

with a cut-off energy of 450 eV. A 1×1×1 Monkhorst Pack k-point grid was utilized for structure optimizations and electronic structure calculations. The conjugate gradient method was employed to fully optimize the positions of the system until all forces on each atom were reduced to less than 0.02 eV/Å. The energy convergence of the whole self-consistent process was determined based on 10^{-5} eV. The gaussian smearing broadening was set to 0.05 eV. [6] The Electrostatic potential (ESP) and molecular structure were visualized using the VESTA.[7] The structure of the MMZ, MMZ-H^+ and diagram of two MMZ-H^+ insertions was optimized with gaussian 16.[1] Geometric optimizations were performed at B3LYP/6-31G(d,p) theoretical level[8] with All with Grimme's dispersion correction of D3 version (Becke-Johnson damping).[9] The size of the structure was calculated with Multiwfn.[10]

Table S1. The comparison between H_3O^+, Li^+, Na^+, K^+, NH_4^+, and Zn^{2+}ions.[11]

Characteristics	H_3O^+	Li^+	Na^+	K^+	NH_4^+	Zn^{2+}
Cation radius	1 Å	0.76 Å	1.02 Å	1.38 Å	1.48 Å	0.74 Å
Hydrated radius	N/A	3.82 Å	3.58 Å	3.31 Å	3.31 Å	4.3 Å

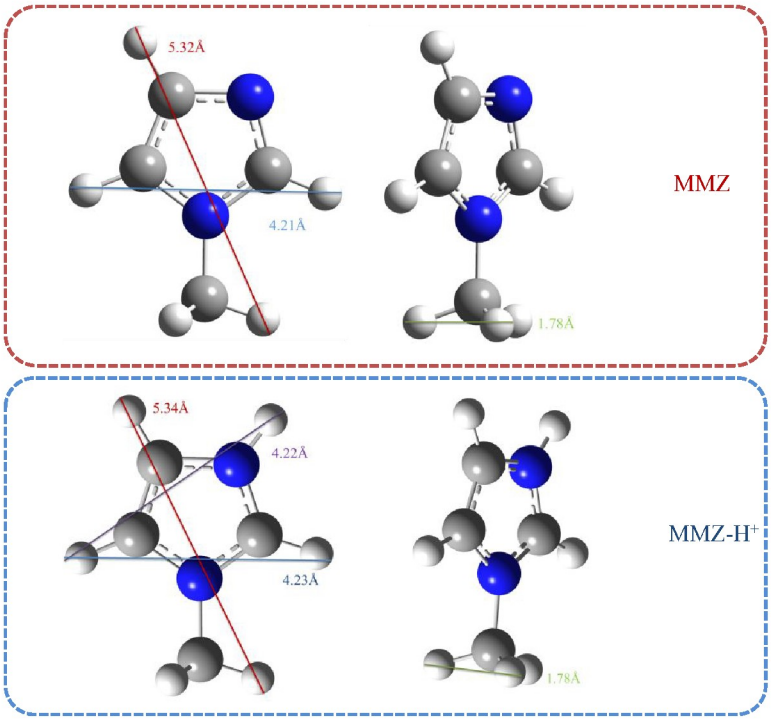

Figure S1. The ionic size of MMZ and MMZ-H^+.

View Article Online
DOI: 10.1039/D5SC02677F

1.5 Calculation details

The theoretical specific capacity of HATN-3CN can be calculated according to the equation as follow.

$$Q = \frac{\mathrm{n}F}{3.6\ \mathrm{M}} \qquad (1)$$

Where n is theoretical electron-transfer numbers of HATN-3CN, F is the Faraday constant, and M is the equivalent molecular weight of HATN-3CN (459.42 g mol^{-1}). Therefore, using Equation 1, the theoretical capacity of HATN-3CN is 350 mAh g^{-1}.

The ionic conductivity a series of electrolytes is calculated following the equations.

$$\sigma = \frac{\mathrm{L}}{\mathrm{RS}} \qquad (2)$$

Where σ refers to the ionic conductivity, L presents the thicknesses of the electrolyte, S is the area of the electrodes, R obtained from the Nyquist plot is the internal resistance of the electrolyte. Calculated values are summarised in Table S3.

Table S3. The ionic conductivity of a series of electrolytes at 25 ˚C.

Solution	Conductivity (mS cm^{-1})	Solution	Conductivity (mS cm^{-1})
0.5M H_2SO_4	219.6	62.5M-10S	106.8
12.5M-10S	193.2	125M-10S	40.6
25M-10S	202.8	250M-10S	37.8
50M-10S	254.4	MMZ in H_2O	4.3

1.6 Preparations of electrode materials

The HATN-3CN electrodes were prepared by mixing organic molecule with carbon black (Ketjen Black) and binder (PVDF) in a mass ratio of 60:30:10 in N-Methylpyrrolidone (NMP) solvent, and coating the slurry onto 12 mm diameter hydrophilic carbon paper and drying at 65 °C under vacuum. The small organic molecule mass load was around 1.5 mg cm^{-2}. The activated carbon (AC) membrane was prepared using the same way with a mass ratio of 80:10:10. When preparing the HATN-3CN electrodes for in situ and ex situ testing, the organic molecule, the Ketjen Black

View Article Online
DOI: 10.1039/D5SC02677F

and PVDF were blended in a mass ratio of 80:10:10 in NMP solvent. After coating the slurry onto 12 mm diameter hydrophilic carbon paper and drying at 65 °C under vacuum. After charging and discharging to the corresponding potential, the HATN-3CN electrodes were rinsed with water and ethanol repeatedly, followed by vacuum drying for ex-situ characterization. It should be noted that ex situ ^{1}H-NMR spectra were tested by dissolving the HATN-3CN electrodes in methyl sulfoxide-d6 (DMSO-d_6) reagent.

1.7 Electrochemical measurements

The half cells were assembled using Swagelok at three-electrode system using a HATN-3CN work electrode, activated carbon counter electrode and KCl-saturated Ag/AgCl ref. electrode, respectively. The full cells were tested at coin cells using HATN-3CN anode and MnO_2 cathode with the voltage range of 0-1.2 V. The pouch cell was designed and fabricated with HATN-3CN, MnO_2, glass microfiber and 0.5 M $MnSO_4$+50M-10S as anode, cathode, separator and electrolyte. Carbon cloth was working as current collector (3 x 3 cm) and tab at the same time. The loading mass of HATN-3CN is 16.2 mg. The linear sweep voltammetry (LSV), cyclic voltammetry (CV) and electrochemical impedance spectroscopy (EIS) measurements were performed on a CHI760e workstation. The EIS was tested with an AC amplitude of 5mV over a frequency ranging from 100 kHz to 0.1 Hz. The galvanostatic charge-discharge (GCD) tests were conducted on LAND-CT2001A battery testing instrument. The Galvanostatic Intermittent Titration Technique (GITT) measurements were carried out with a pulse of 2 min and a rest interval 5 min in a current density of 0.1 A g^{-1}.

2. Synthetic Procedures

2.1 Synthesis of Diquinoxalino[2,3-a:2',3',-c]phenazine-2,8,14-tricarbonitrile (HATN-3CN)

The HATN-3CN was synthesized by reference to the previously reported work.[12] ^{1}H NMR (400 MHz, DMSO-d_6): δ 9.21, 9.18, 8.77, 8.71, 8.69, 8.73, 8.42, 8.41. HR-MS: m/z calculated for C27H9N9: 460.1; $[M + H]^+$ found: 460.10.

View Article Online
DOI: 10.1039/D5SC02677F

2.2 Preparation of 0.5 M H_2SO_4-MMZ electrolytes

Aqueous electrolytes were obtained by mixing MMZ solution in 0.5 M H_2SO_4 with stirring at room temperature. Electrolytes with different MMZ contents were shown in the table S2.

Table S2. The composition of a series of 0.5 M H_2SO_4-MMZ electrolytes.

name	MMZ mL	0.5M H_2SO_4 mL	pH	mole ratio (MMZ: H_2SO_4)
0.5M H_2SO_4	0	2	0.19	0:100
12.5M-10S	0.1	2	0.24	12.5:10
25M-10S	0.2	2	2.13	25:10
37.5M-10S	0.3	2	6.94	37.5:10
50M-10S	0.4	2	7.46	50:10
62.5M-10S	0.5	2	7.79	62.5:10
125M-10S	1	2	7.87	125:10
250M-10S	2	2	8.13	250:10
MMZ in H_2O	0.4	2 (H_2O)	10.81	50:0

Table S4. The viscosity of a series of electrolytes at 25ºC.

Solution	MMZ in H_2O	12.5M-10S	25M-10S	37.5M-10S	50M-10S	62.5M-10S	125M-10S	250M-10S
Viscosity/mPa*s	1.288	1.916	2.08	2.172	2.491	2.784	3.143	3.964

View Article Online
DOI: 10.1039/D5SC02677F

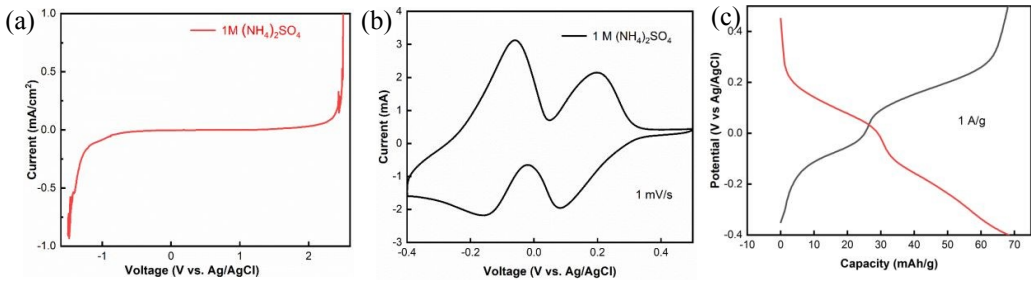

Figure S2. (a) The LSV curve and (b) CV curves (c) charge-discharge curve of HATN-3CN electrode in 1 M $(NH_4)_2SO_4$.

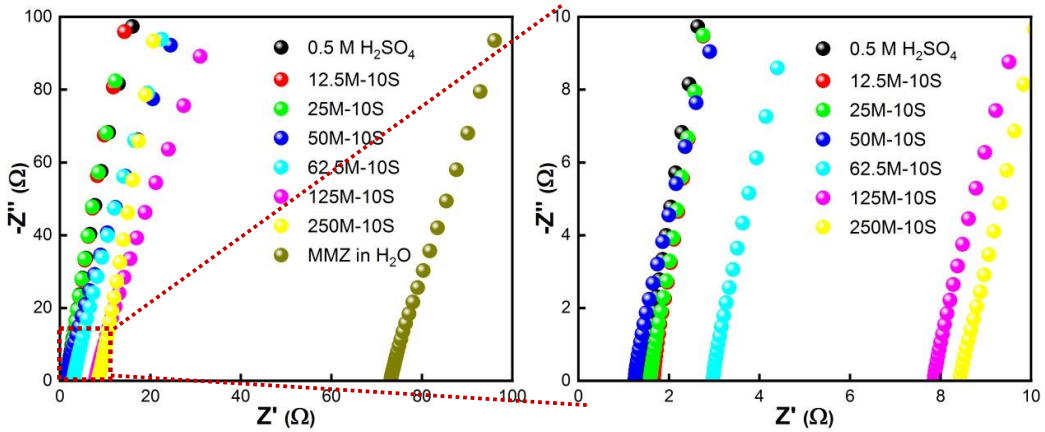

Figure S3. Nyquist plots of a series of electrolytes to obtain the ion conductivities.

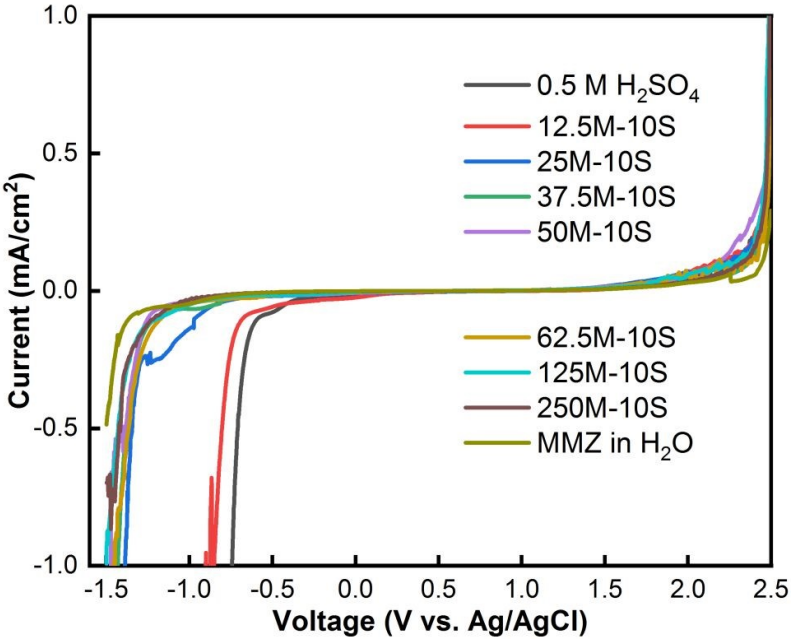

Figure S4. LSV curves of a series of electrolytes.

View Article Online
DOI: 10.1039/D5SC02677F

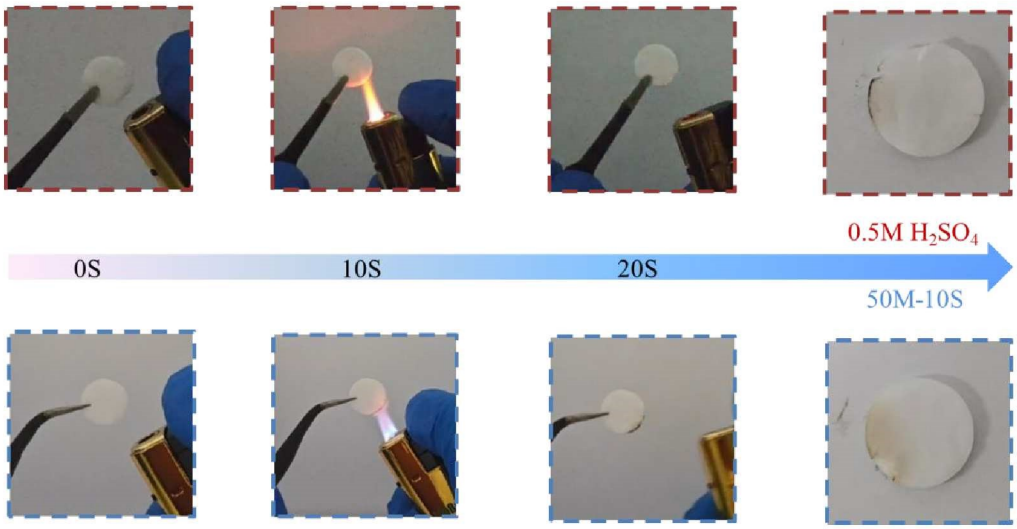

Figure S5. Combustion process of 0.5 M H_2SO_4 and 50M-10S electrolytes in 0-20 seconds.

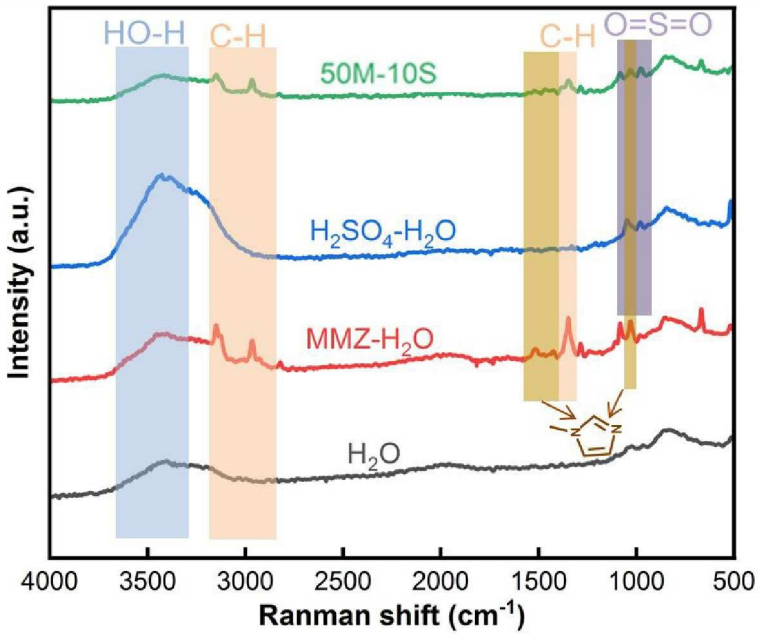

Figure S6. Raman spectra of contents in 50M-10S electrolyte.

View Article Online
DOI: 10.1039/D5SC02677F

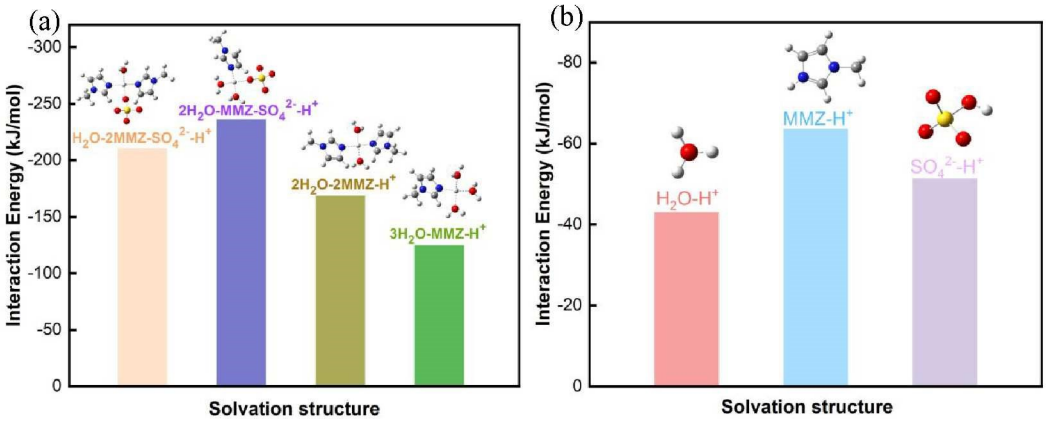

Figure S7. The binding energy of (a) a series of contents and (a) several configurations of electrolytes.

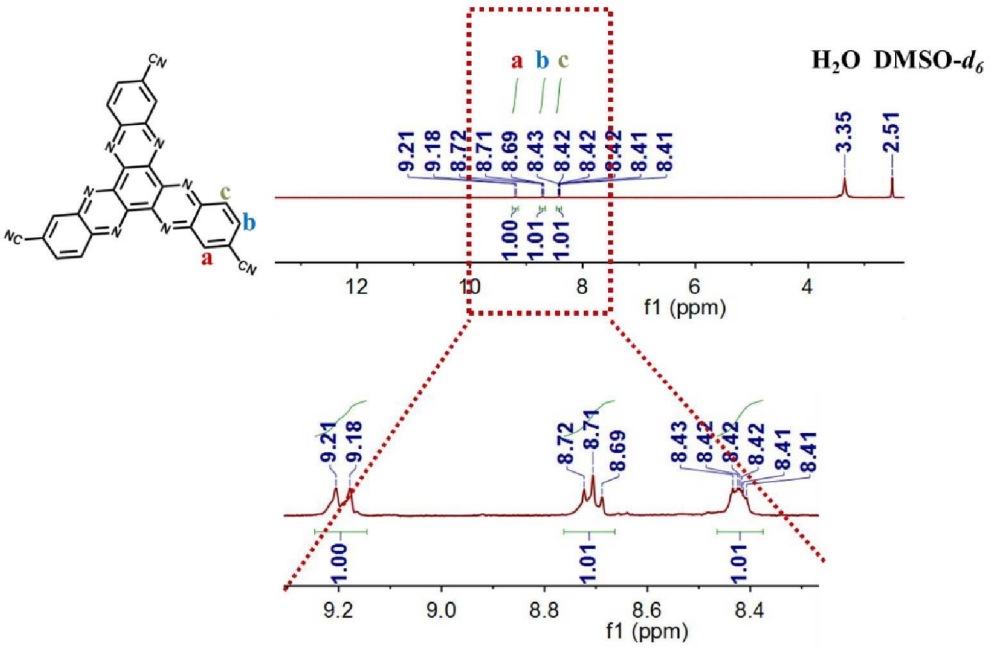

Figure S8. The ^{1}H NMR spectrum of HATN-3CN.

View Article Online
DOI: 10.1039/D5SC02677F

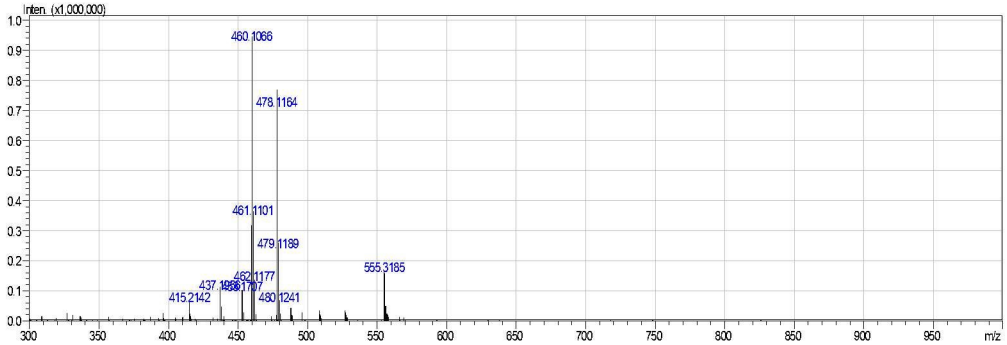

Figure S9. HR-MS mass spectroscopy of HATN-3CN.

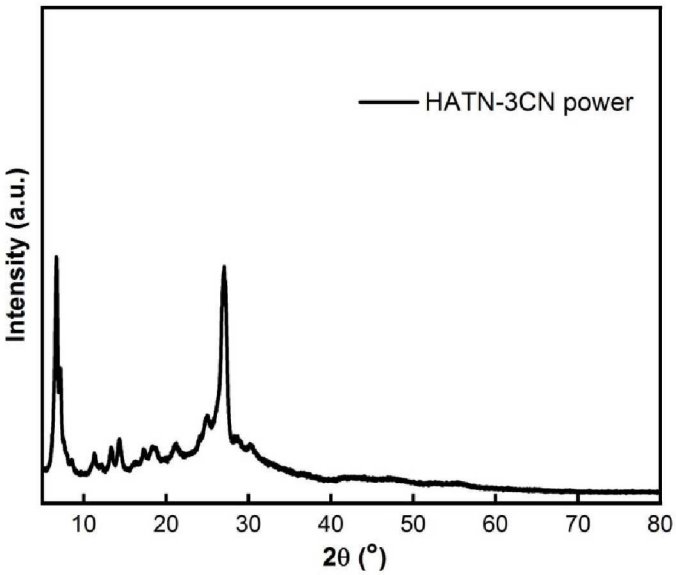

Figure S10. PXRD of HATN-3CN power.

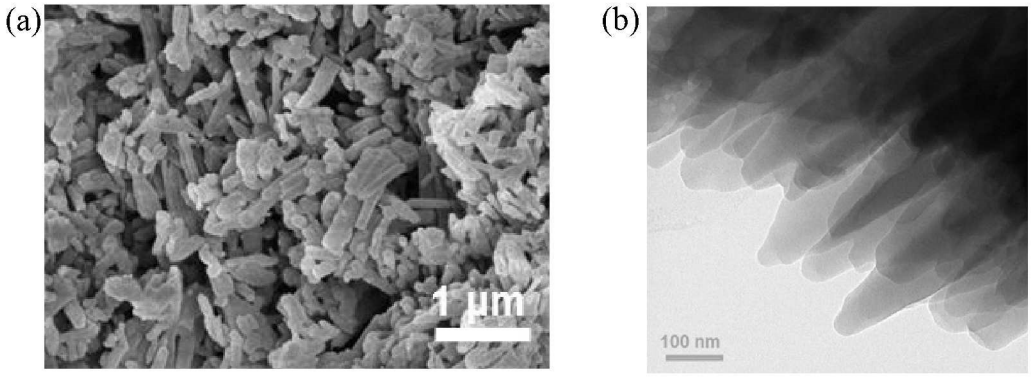

Figure S11. SEM images(a) and TEM images (b) of HATN-3CN power.

View Article Online
DOI: 10.1039/D5SC02677F

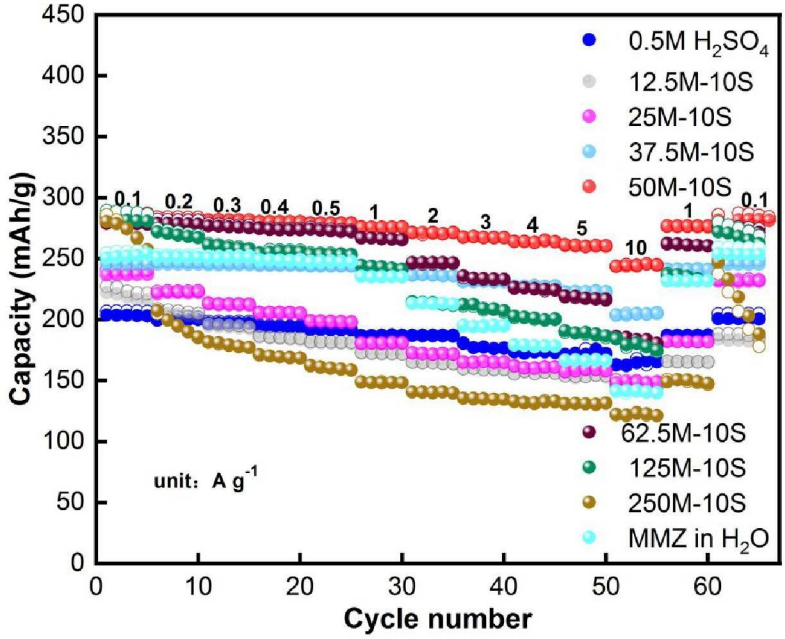

Figure S12. The rate performance of HATN-3CN under different ratios MMZ of electrolyte.

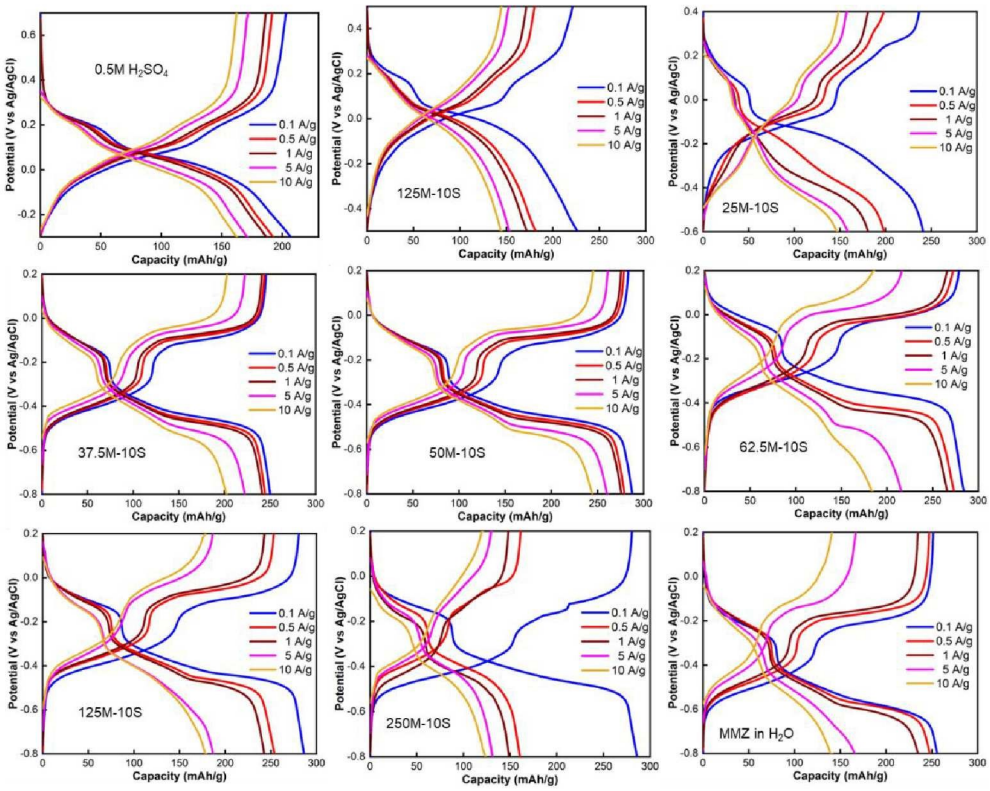

Figure S13. The charge-discharge curves of HATN-3CN electrode in a series of electrolytes.

View Article Online
DOI: 10.1039/D5SC02677F

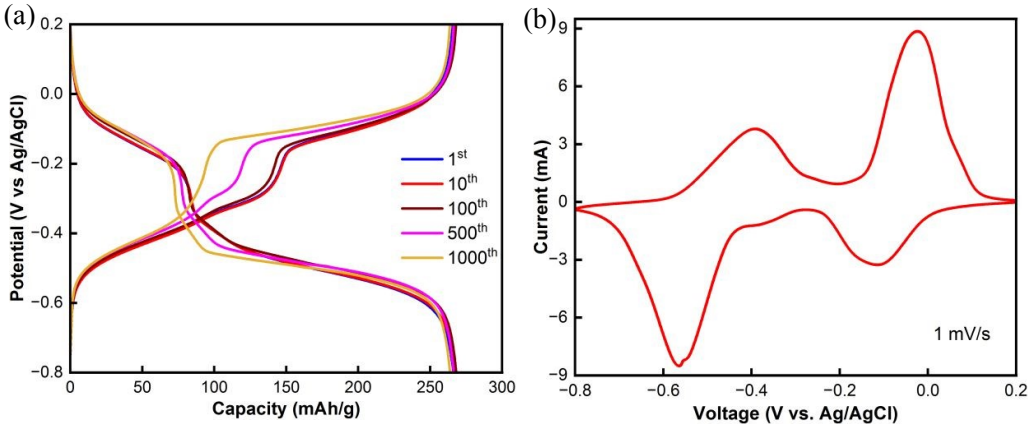

Figure S14. (a) The GCD curves of HATN-3CN of 1st, 10th, 100th, 500th and 1000th cycle and (b) CV curve of HATN-3CN after 1000 cycles in 50M-10S electrolyte.

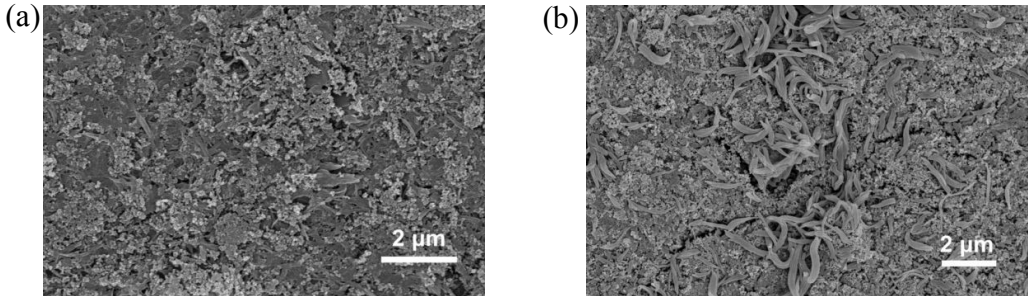

Figure S15. SEM images of HATN-3CN electrode in (a) initial state and (b) after 1000 cycles.

View Article Online
DOI: 10.1039/D5SC02677F

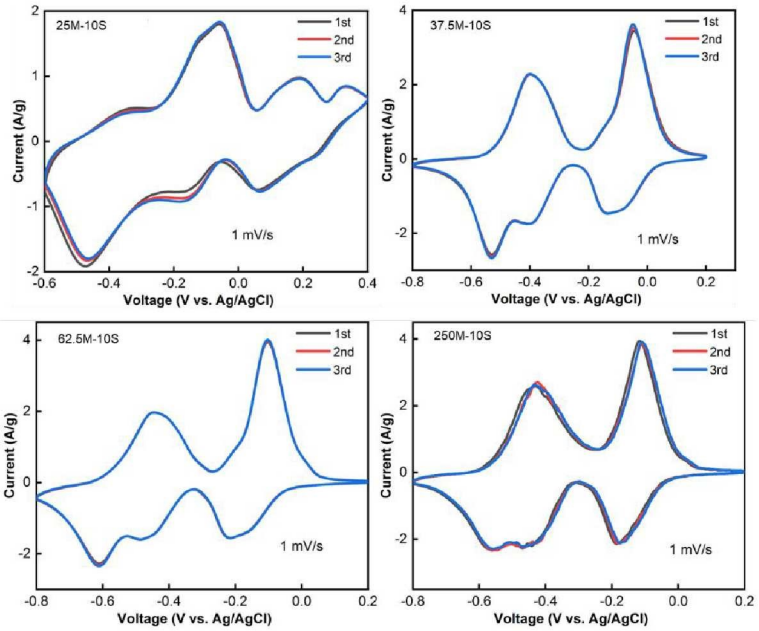

Figure S16. The CV curves of HATN-3CN electrode in different electrolytes.

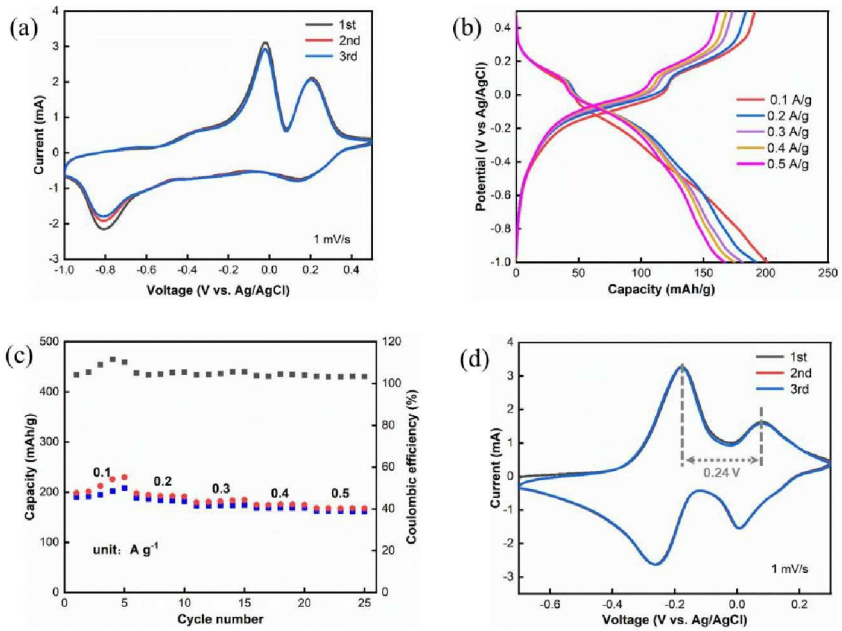

Figure S17. (a) The CV curve, (b) charge-discharge curve and (c) rate curve of HATN-3CN electrode in 1 M DMMZC electrolyte. (d) CV curves of HATN-3CN electrode in MTZ-H_2SO_4 electrolyte.

Note: MTZ-H_2SO_4 electrolyte was obtained by mixing 1 mL of MTZ with 1 mL of H_2O and 0.2 mL of 0.5 M H_2SO_4.

View Article Online
DOI: 10.1039/D5SC02677F

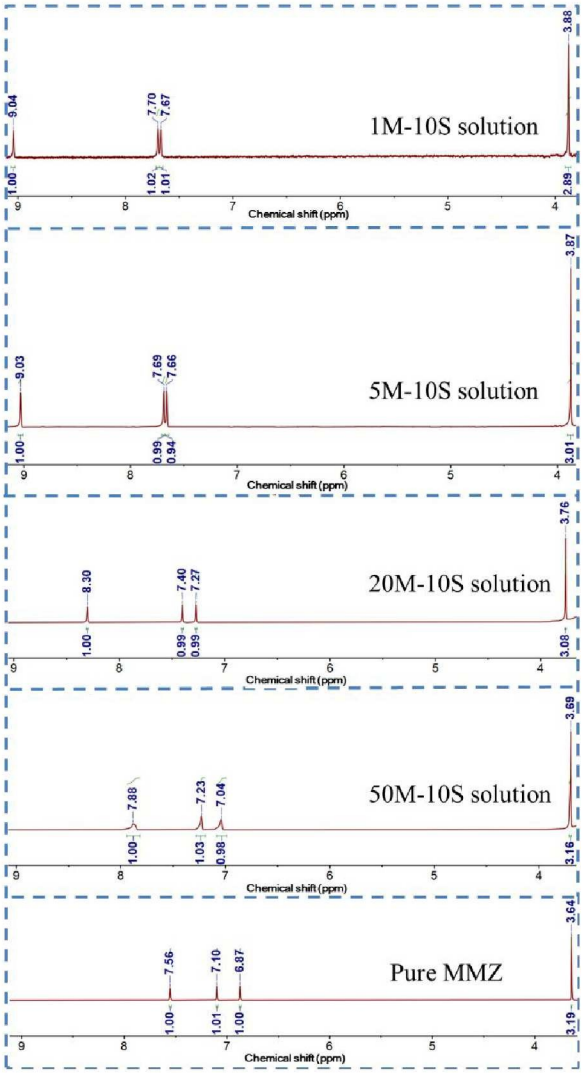

Figure S18. (a) ^{1}H-NMR spectra of different molar ratios of MMZ/H_2SO_4. The solvents used for the ^{1}H-NMR spectra were DMSO-d_6.

Note: MMZ/H_2SO_4 solutions were configured similarly to the M-S electrolyte. Taking the 1M-10S solution as an example, the solution was obtained by mixing 8 μL of MMZ with 2 mL of 0.5 M H_2SO_4, and the mol ratio of MMZ to $H_2SO_4$was 1:10. The chemical shifts of the imidazolium ion's four hydrogens (m, n, o, p likely the one labeled in figure 4f) are shown from left to right in the figure S18.

View Article Online
DOI: 10.1039/D5SC02677F

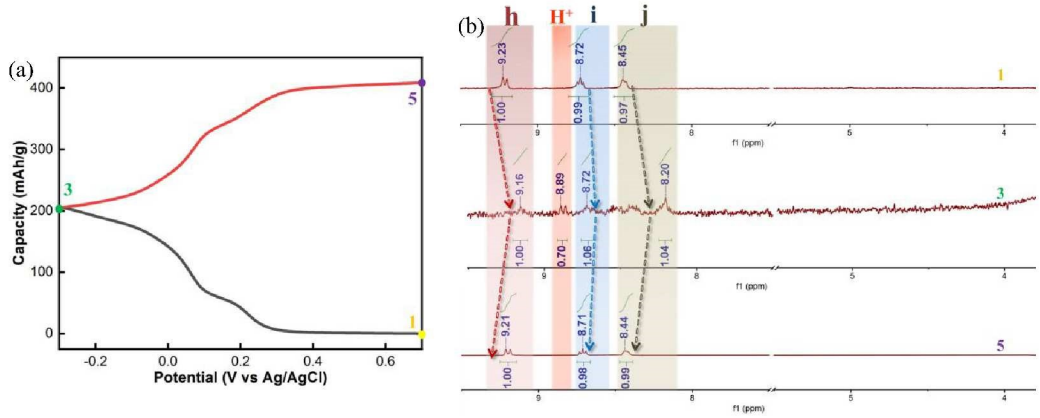

Figure S19. (a) Indication of different charge and discharge states, and (b) Ex situ ^{1}H-NMR spectra of HATN-3CN electrodes in 0.5 M H_2SO_4.

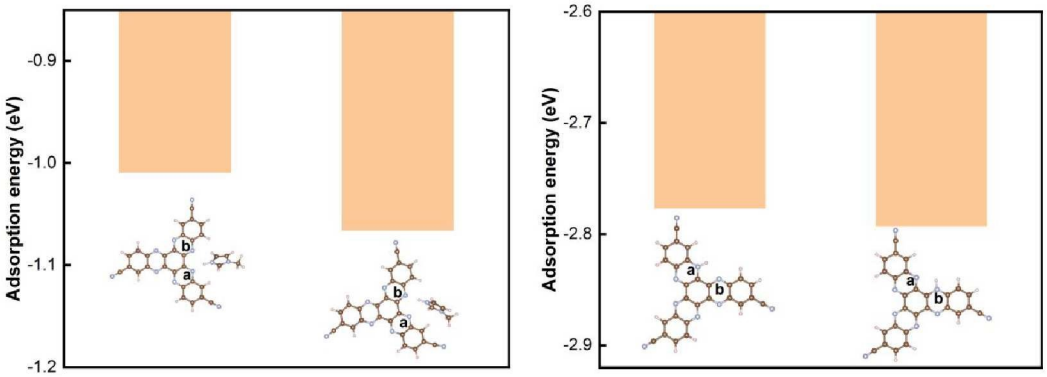

Figure S20. The adsorption energy calculations of different sites.

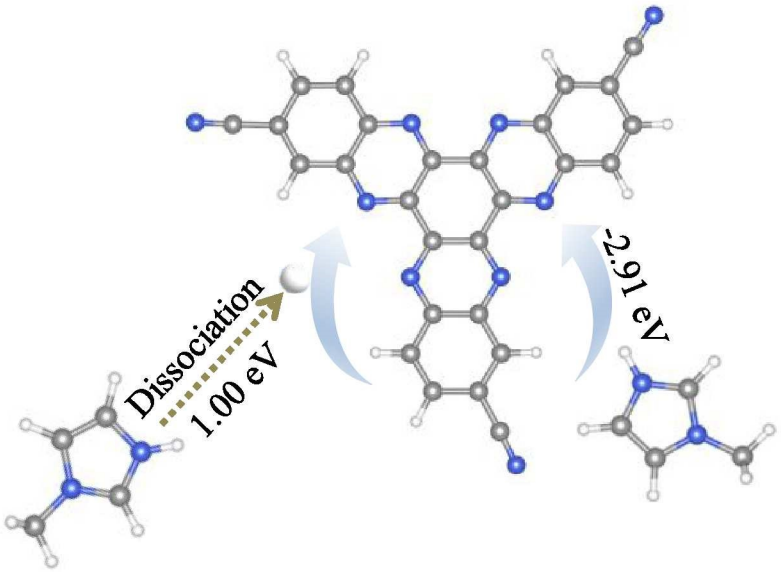

Figure S21. The energy calculation for different insertion methods.

View Article Online
DOI: 10.1039/D5SC02677F

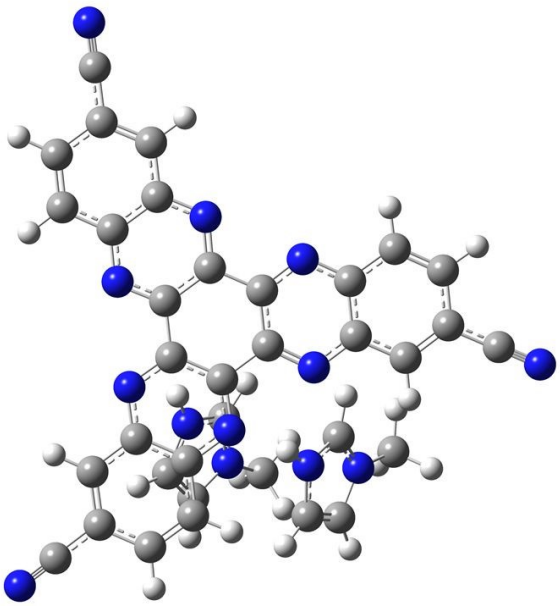

Figure S22. Structural optimization diagram of two MMZ-H^+ insertions.

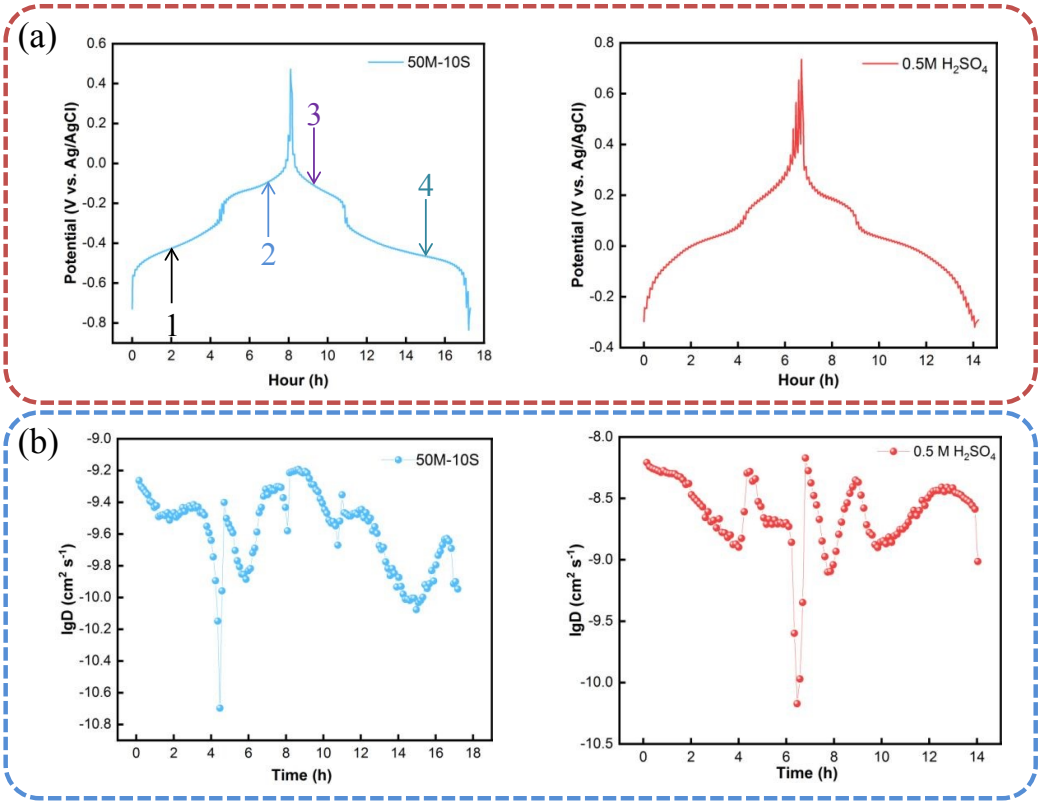

Figure S23. (a) GITT profiles of HATN-3CN electrode and (b) ion diffusion coefficients in 50M-10S electrolyte and 0.5 M H_2SO_4.

View Article Online
DOI: 10.1039/D5SC02677F

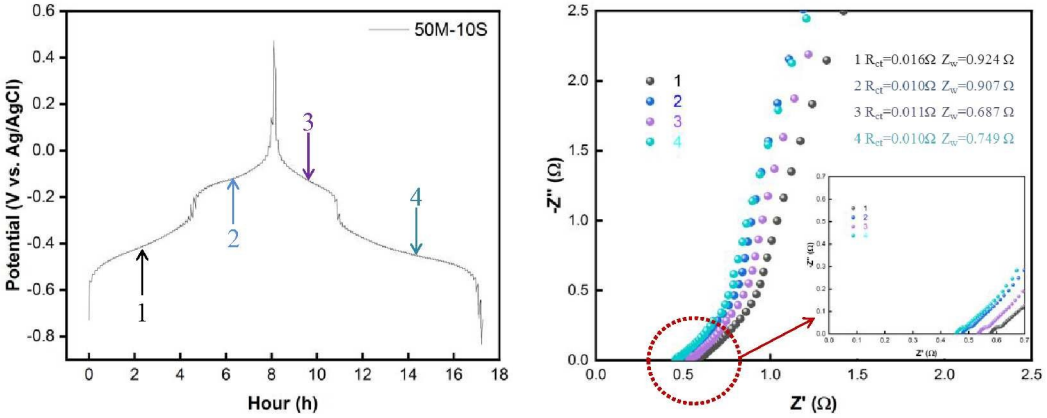

Figure S24. The EIS test of HATN-3CN electrode in 50M-10S electrolyte.

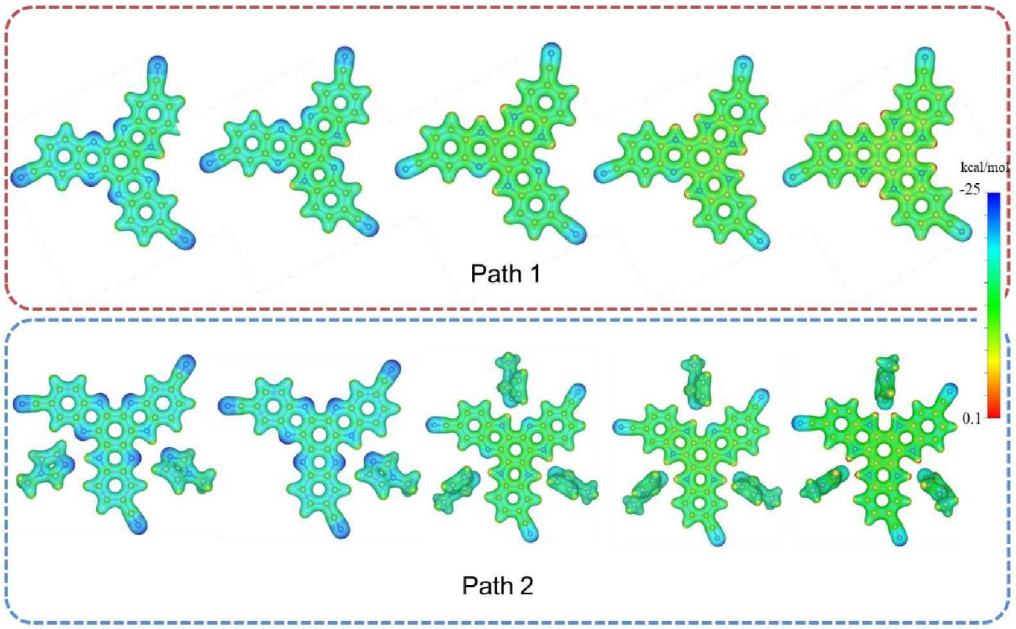

Figure S25. Calculation of MESP distribution of HATN-3CN.

View Article Online
DOI: 10.1039/D5SC02677F

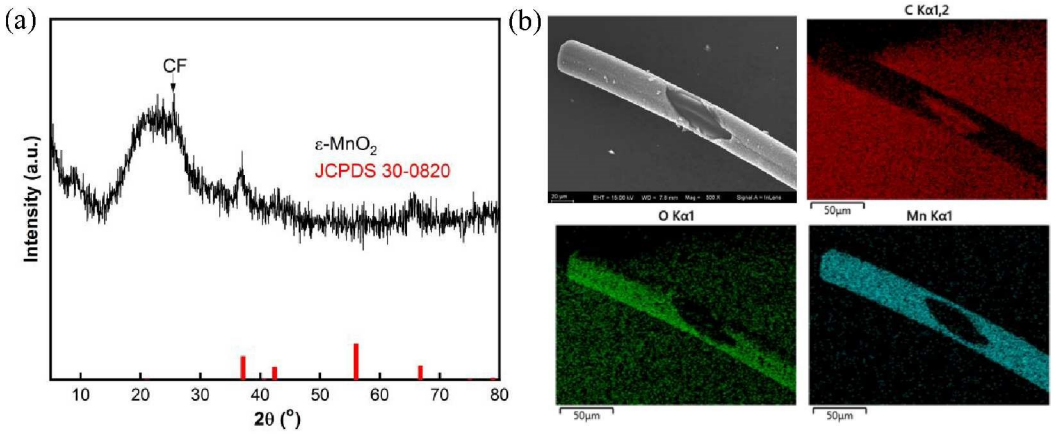

Figure S26. Physical characterizations of MnO_2. (a) XRD pattern. (b) SEM images and EDS elemental mapping images for MnO_2 in carbon fiber.

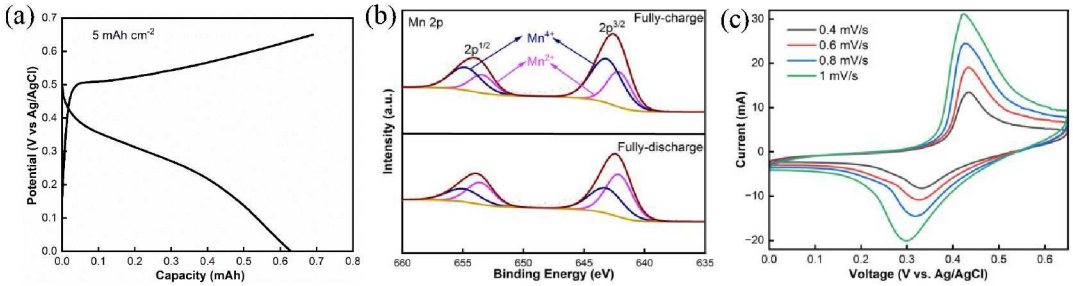

Figure S27. (a) The charge-discharge curves and (b) XPS change during the charging and discharge process and (c) CV curves of MnO_2 electrode.

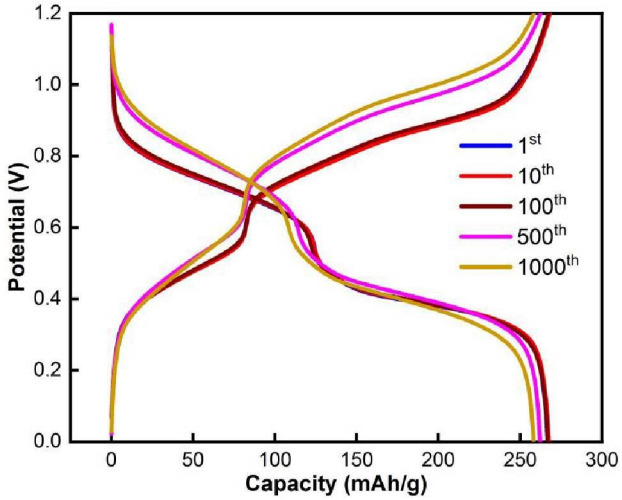

Figure S28. The GCD curves of HATN-3CN of 1st, 10th, 100th, 500th and 1000th cycle of full cell after 1000 cycles in 0.5 M $MnSO_4$ + 50M-10S electrolyte.

View Article Online
DOI: 10.1039/D5SC02677F

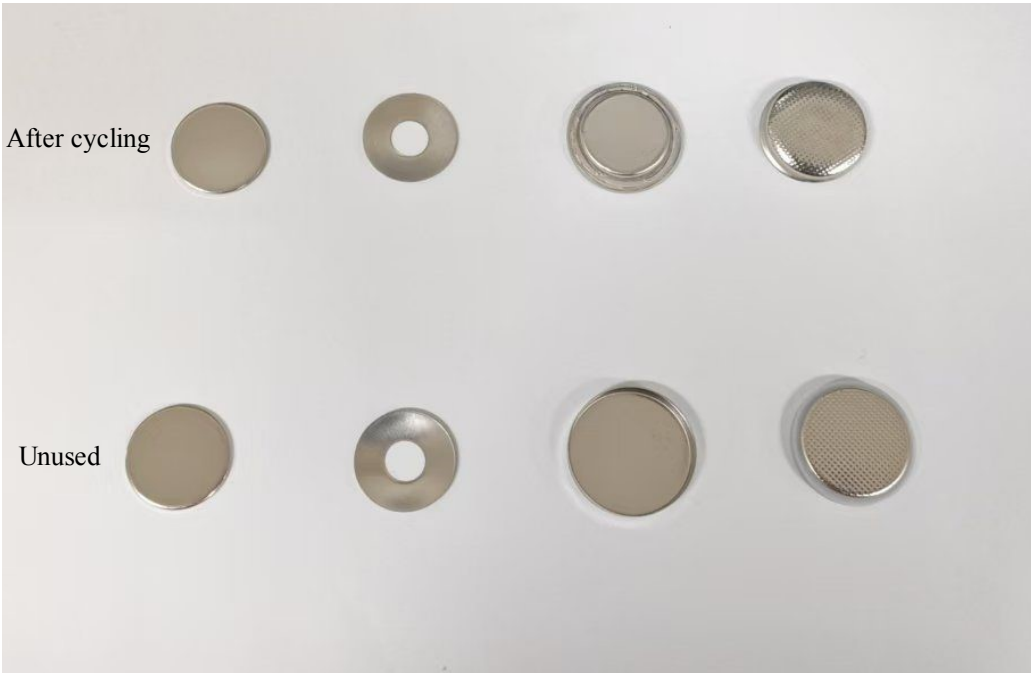

Figure S29. The digital image of battery cases after cycling in 0.5 M $MnSO_4$ +50M-10S electrolyte (top) and unused (bottom).

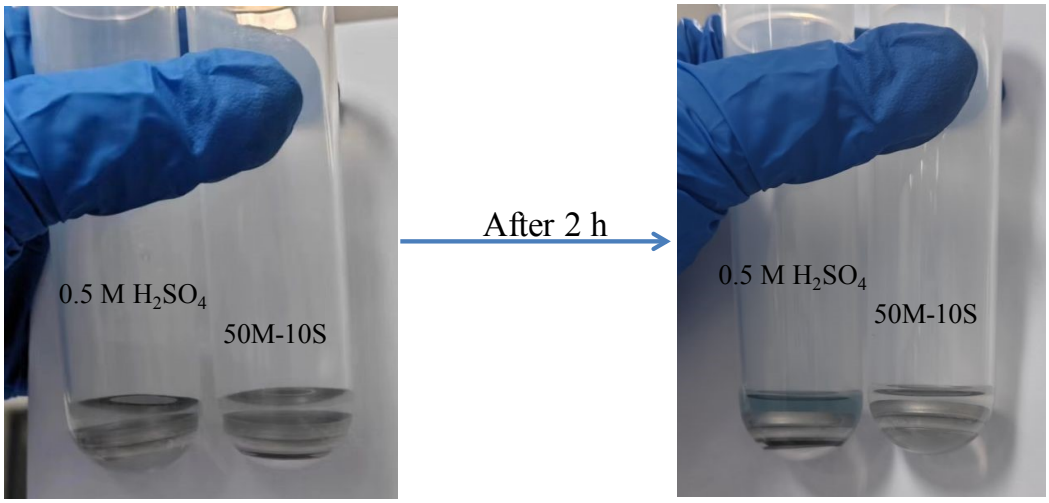

Figure S30. The digital image of components of 2032 coin cell soaked in different circumstances.

View Article Online
DOI: 10.1039/D5SC02677F

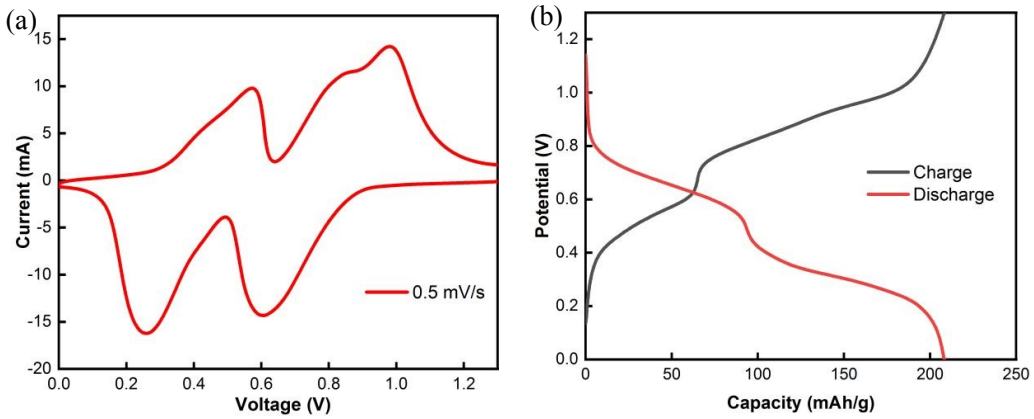

Figure S31. CV (a) and GCD curves (b) of HATN-3CN//MnO_2 pouch cell.

Note: The pouch cell was designed and fabricated with HATN-3CN, MnO_2, glass microfiber and 0.5M $MnSO_4$+50M-10S as anode, cathode, separator and electrolyte. Carbon cloth was working as current collector (3 x 3 cm) and tab at the same time. The loading mass of HATN-3CN is 16.2 mg.

View Article Online
DOI: 10.1039/D5SC02677F

Table S5. Comparison of recently reported proton battery electrolytes with full cell configuration.

Electrodes	Electrolytes	Ions type	Cycling stability (specific capacity/based on; current density; cycles; capacity retention)	Reference
HATN-3CN//MnO_2	0.5 M $MnSO_4$ in 50M-10S electrolyte	MMZ-H^+ & H^+	266.6mAh g^{-1}/anode, 1 A g^{-1} , 1000, 97 %	This work
PTO//MnO_2	2.0 M H_2SO_4 +2.0 M $MnSO_4$	H^+	203.4 mAh g^{-1}/-, 3 A g^{-1} , 400, 88 %	Ref.[13]
PTO//MnO_2@GF	2.0 M H_2SO_4 +2.0 M $MnSO_4$	H_3O^+	150 mAh g^{-1}/anode, 2.5 C , 5000, 80 %	Ref.[14]
MoO3@TiO_2//MnO_2	1.0 M H_2SO_4 +1.0 M $MnSO_4$	H^+	~200 mAh g^{-1}/anode, 10 A g^{-1}, 500, 80 %	Ref.[15]
ALO // MnO2@CF	2 M H_2BF_4 +2M $MnBF_4$	H^+	145 mAh g^{-1}/anode, 5 A g^{-1} , 300, 80 %	Ref.[16]
AC//VPO_4F	H_3PO_4 in MeCN	H^+	42 mAh g^{-1}/cathode, 0.2 A g^{-1}, 300, 72%	Ref.[17]
PTCDI//Ni-APW	1.0M $(NH_4)_2SO_4$	NH_4^+	35 mAh g^{-1}/total mass, 0.12 A g^{-1},1000, 67%	Ref.[7]
PTCDI//KVO	22 M KCF_3SO_3 WiSE	K^+	~70 mAh g^{-1}/cathode, 10 C, 20000, 77.3%	Ref.[18]
Zn//PTD-1	2 M $ZnSO_4$	H^+ & SO_4^{2-}	~125mAh g^{-1}/cathode, 1 A g^{-1}, 4000, 82.5%	Ref.[19]
Zn//6CN-HAT@MXene	2 M $Zn(CF_3SO_3)_2$	Zn^{2+} & H^+	200 mAh g^{-1}/cathode, 5 A g^{-1}, 5000, 90%	Ref.[20]

View Article Online
DOI: 10.1039/D5SC02677F

PAQS//Ni(OH)$_2$	10 M KOH	K^+ & H^+	180 mAh g^{-1}/-, 0.2 A g^{-1}, 1350, 88%	Ref.[21]
HPP-COF// CoNi-LDH	1 M NaOH	Na^+	119.6 mAh g^{-1}/ anode, 30 A g^{-1},10000, 70.6%	Ref.[22]

View Article Online
DOI: 10.1039/D5SC02677F

Reference

[1] G. W. T. M. J. Frisch, H.B. Schlegel, G.E. Scuseria, M.A. Robb, J.R. Cheeseman, G. Scalmani, V. Barone, G.A. Petersson, H. Nakatsuji, X. Li, M. Caricato, A.V. Marenich, J. Bloino, B.G. Janesko, R. Gomperts, B. Mennucci, D.J. Hratch. , Revision C.01 Gaussian, Inc., Wallingford CT Revision C.01 Gaussian, Inc., Wallingford CT (2016).

[2] F. U. S. Yong-Lei Wang, Sergei Glavatskih, Oleg Antzutkin, Aatto Laaksonen., Atomistic insight into orthoborate-based ionic liquids: Force field development and evaluation, J. Phys. Chem. B 118 (2014) 8711-8723.

[3] T. M. Mark James Abraham, Roland Schulz, Szilárd Páll, Jeremy C. Smith, Berk Hess, Erik Lindahl., High performance molecular simulations through multi-level parallelism from laptops to supercomputers., SoftwareX 1(2015).

[4] Kresse, G. & Furthmüller, J. Efficiency of ab-initio total energy calculations for metals and semiconductors using a plane-wave basis set. Comput. Mater. Sci. 6, 15–50 (1996).

[5] Perdew, J. P., Burke, K. & Ernzerhof, M. Generalized gradient approximation made simple. Phys. Rev. Lett. 77, 3865 (1996).

[6] Zhao, K. et al. Single-ion chelation strategy for synthesis of monodisperse Pd nanoparticles anchored in MOF-808 for highly efficient hydrogenation and cascade reactions. Nanoscale 14, 10980–10991 (2022).

[7] Momma, K.; Izumi, F. VESTA: A Three-Dimensional Visualization System for Electronic and Structural Analysis. *Journal of Applied crystallography* 2008, *41* (3), 653–658.

[8] Tirado-Rives, J.; Jorgensen, W. L. Performance of B3LYP Density Functional Methods for a Large Set of Organic Molecules. *Journal of chemical theory and computation* 2008, *4* (2), 297–306.

[9] Grimme, S.; Bannwarth, C.; Shushkov, P. A Robust and Accurate Tight-Binding Quantum Chemical Method for Structures, Vibrational Frequencies, and Noncovalent Interactions of Large Molecular Systems Parametrized for All Spd-Block Elements (Z = 1–86). *J. Chem. Theory Comput.* 2017, *13* (5), 1989–2009.

[10] Lu, T.; Chen, F. Multiwfn: A Multifunctional Wavefunction Analyzer. *Journal of computational chemistry* **2012**, *33* (5), 580–592.

View Article Online
DOI: 10.1039/D5SC02677F

[11] Wu X, Qi Y, Hong J J, et al. Rocking-Chair Ammonium-Ion Battery: A Highly Reversible Aqueous Energy Storage System[J]. Angewandte Chemie International Edition, 2017, 56(42): 13026-13030.

[12] Wang X, Yang Y, Lai C, et al. Dense-Stacking Porous Conjugated Polymer as Reactive-Type Host for High-Performance Lithium Sulfur Batteries[J]. Angewandte Chemie International Edition, 2021, 60(20): 11359-11369.

[13] Wu S, Guo H, Su Z, et al. Suppressed Manganese Oxides Shuttling in Acidic Electrolytes Extends Shelf-Life of Electrolytic Proton Batteries[J]. Advanced Functional Materials, 2024, 34(28): 2315706.

[14] Guo Z, Huang J, Dong X, et al. An organic/inorganic electrode-based hydronium-ion battery[J]. Nature Communications, 2020, 11(1): 959.

[15] Wang C, Zhao S, Song X, et al. Suppressed Dissolution and Enhanced Desolvation in Core–Shell MoO3@TiO2 Nanorods as a High-Rate and Long-Life Anode Material for Proton Batteries[J]. Advanced Energy Materials, 2022, 12(19): 2200157.

[16] Sun T, Du H, Zheng S, et al. High Power and Energy Density Aqueous Proton Battery Operated at −90 °C[J]. Advanced Functional Materials, 2021, 31(16): 2010127.

[17] Liao M, Cao Y, Li Z, et al. VPO4F Fluorophosphates Polyanion Cathodes for High-Voltage Proton Storage[J]. Angewandte Chemie International Edition, 2022, 61(32): e202206635.

[18] Liang G, Gan Z, Wang X, et al. Reconstructing Vanadium Oxide with Anisotropic Pathways for a Durable and Fast Aqueous K-Ion Battery[J]. ACS Nano, 2021, 15(11): 17717-17728.

[19] Wang N, Guo Z, Ni Z, et al. Molecular Tailoring of an n/p-type Phenothiazine Organic Scaffold for Zinc Batteries[J]. Angewandte Chemie International Edition, 2021, 60(38): 20826-20832.

[20] Zhao D, Li Z, Xu D, et al. Multiple Redox-Active Cyano-Substituted Organic Compound Integrated with MXene Nanosheets for High-Performance Flexible Aqueous Zn-Ion Battery[J]. Advanced Functional Materials, 2024, 34(25): 2316182.

[21] Liang Y, Jing Y, Gheytani S, et al. Universal quinone electrodes for long cycle life aqueous r echargeable batteries[J]. Nature Materials, 2017, 16(8): 841-848.

[22] Lin Y, Cui H, Liu C, et al. Inside Back Cover: A Covalent Organic Framework as a Long-life and High-Rate Anode Suitable for Both Aqueous Acidic and Alkaline Batteries [J].

View Article Online
DOI: 10.1039/D5SC02677F

Angewandte Chemie International Edition, 2023, 62(14): e202302702.